JOURNAL OF SPACECRAFT AND ROCKETS
Vol. 38, No. 3, May–June 2001

Overview and Summary of Results and Significant Findings from the CIRRIS-1A Experiment

J. O. Wise,* D. R. Smith,† N. B. Wheeler,† M. Ahmadjian,‡ and R. M. Nadile†
U.S. Air Force Research Laboratory, Hanscom Air Force Base, Massachusetts 01731
and
B. F. Sullivan§
Boston College, Chestnut Hill, Massachusetts 02467

The cryogenic infrared radiance instrumentation for shuttle (CIRRIS) experiment was flown onboard STS-39 from 29 April to 1 May 1991. A comprehensive set of spectral and spatial infrared data of atmospheric and Earth terrain data was collected by an interferometer and radiometer. The mission occurred during a major geomagnetic storm ($K_p \geq 5$), and as a result, a substantial amount of spectral data on bright auroral backgrounds were collected in the midnight sector of the auroral oval. The coincidental timing of the CIRRIS mission, only a few weeks before the eruption of Mount Pinatubo (June 1991), substantially increased the value of the stratospheric data from CIRRIS, which now serves as a clean atmosphere baseline against which various post-Pinatubo observations can be compared to assess the short- and long-term effects of a major volcanic eruption on the stratosphere. In addition, there were a number of unexpected and important scientific discoveries that resulted from analysis of the CIRRIS high-resolution Earthlimb emission spectra including the identification of an important new class of non-local thermodynamic equilibrium emissions resulting from highly rotationally excited diatomic species (OH, NO and NO^+) in the mesosphere and thermosphere. These nonthermal rotational emissions were observed for both day and nighttime conditions and were not included in or predicted by existing atmospheric models before the CIRRIS flight. A brief overview of the instrumentation and data collection methods is presented. A general review of the CIRRIS data and a summary of the most significant findings previously reported by various groups are also presented.

Introduction

Scientific Objectives

THIS paper summarizes the results and major findings from the cryogenic infrared radiance instrumentation for shuttle (CIRRIS-1A) experiment that was flown onboard STS-39 between 29 April and 1 May 1991. This study consisted of a global infrared remote sensing survey that sampled the atmosphere from the nadir up through the Earthlimb to shuttle altitudes of 260 km in the 2.5–25 μm wavelength region. The primary objective of this experiment was to obtain simultaneous spectral and spatial measurements of atmospheric emissions for altitudes between 0 and 150 km. Atmospheric species of interest included water, hydroxyl, nitric oxide, ozone, and carbon dioxide during day and night under various levels of geomagnetic activity. Observations covered a range of latitudes from approximately −68 to +68 deg during moderate to active geomagnetic activity ($K_p = 3$–7) and also when bright aurora were observed. Data were collected from numerous strong atmospheric emitters, such as OH at 2.7 μm and CO_2 at 4.3 and 15 μm, NO at 5.3 μm, O_3 at 9.6 μm, and H_2O at 6.3 μm and in the long wavelength infrared (LWIR) region. Many other trace species were also measured, such as CFC-11 and CFC-12, HNO_3, CH_4, and CO. Data were taken simultaneously by three infrared (IR) instruments: 1) an interferometer with an eight position filter wheel, 2) a filter radiometer with 7 wide and narrow bandpass filters, and 3) a fixed-filter radiometer with a bandpass in the 2.7-μm region. The radiometer and interferometer individually have yielded many new discoveries, which will be reviewed in later sections of this paper. However, together they provide a much more comprehensive picture of the global variations in composition, temperature, and energetic processes than would either instrument alone. Besides confirmation of observed phenomena between instruments, the radiometer detected highly resolved variations in emission with space and time, whereas the interferometer could diagnose the relative contributions from simultaneous species within each broad passband of the radiometer. In addition, there were several other clear benefits to having simultaneous interferometer and radiometer data. In the lower thermosphere, emissions in the passband of the 2.7-μm radiometer were significantly enhanced during aurora. As a result, this radiometer served as an important diagnostic tool (along with the two visible photometers) for daytime and nighttime high-latitude particle precipitation in the lower thermosphere that cause compositional changes in the upper atmosphere, such as CO_2 vertical lift, or enhanced emissions from NO in the 6–9-μm window region and NO^+ in the 4.3-μm band. The 2.7-μm radiometer was also useful as an indirect monitor for other atmospheric emissions as well. For example, near the mesopause, variations in the 2.7-μm passband could also be directly correlated with similar changes in the pure-rotational emissions from OH in the 11–13-μm window. As a consequence of the fixed-filter design, the 2.7-μm radiometer was active whenever the CIRRIS instrument was turned on, and thus, it collected data continuously throughout the entire CIRRIS mission.

Background

The CIRRIS-1A experiment is part of a large Department of Defense (DOD) program to explore the chemistry of the Earth's upper atmosphere. The data collected by this program support the development of space defense systems that use IR and other electro-optical sensors to detect targets in the boost phase, postboost phase, orbiting, or in the reentry phase of the mission. To be able to passively detect and track these targets at long ranges, systems must be able to discriminate the spectral signature of the target emissions (IR, visible, and ultraviolet) from emissions produced by atomic and molecular species in the Earth's atmosphere. Sensor systems designers must take into account these atmospheric backgrounds to determine optimum wavelength regions where sensors are able to see through the atmosphere and where targets of interest emit enough photons to provide adequate signal to noise and sufficient

Received 13 December 1999; revision received 25 July 2000; accepted for publication 29 July 2000.

*Research Physicist, Space Physics Models Branch, Space Vehicles Directorate (VSBP).
†Research Physicist, Backgrounds Characterization Branch, Space Vehicles Directorate (VSBC).
‡Research Physicist, Space Vehicles Directorate (VSOP). Senior Member AIAA.
§Senior Research Scientist, Institute for Scientific Research. Senior Member AIAA.

target to atmosphere background contrast. CIRRIS and other experiments conducted by the DOD and the civilian community provide the experimental data for system designers as well as for collateral research and global atmospheric models.

Before the CIRRIS experiment, there had been few spectral measurements of the quiescent upper atmosphere in the IR, especially for sunlit conditions. Although the U.S. Air Force had conducted a number of IR spectral rocket probes during aurorally disturbed conditions,[1–3] these provided little insight into the important daytime chemistry of the mesosphere and thermosphere. One of the most carefully studied IR measurements was the spectral IR experiment (SPIRE), which was flown on a rocket launched from Poker Flat, Alaska, close to sunrise in September of 1977. Although SPIRE did not measure the influence of geomagnetic activity on IR emissions, it was the first IR experiment to observe altitude resolved atmospheric emissions on the diurnal variations in the mesosphere and lower thermosphere. Results of this experiment have been reported by Sharma et al.[4] and Stair et al.[5] However, note that although SPIRE obtained data for both night and daytime conditions, the measurements were centered near the dawn terminator and, thus, did not sample late morning, midday, or afternoon conditions. As a result of this, several important daytime enhancements (such as for NO at 5.3 μm) that were easily discerned by CIRRIS were not observed by the SPIRE sensor. Figure 1 summarizes the species and approximate tangent altitude ranges over which these species were observed by CIRRIS-1A sensors.

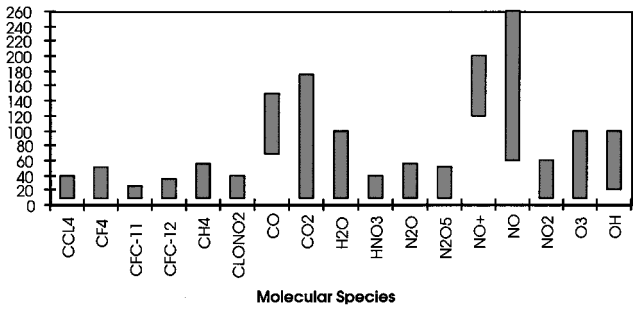

Fig. 1 Summary of molecular species observed by the CIRRIS experiment.

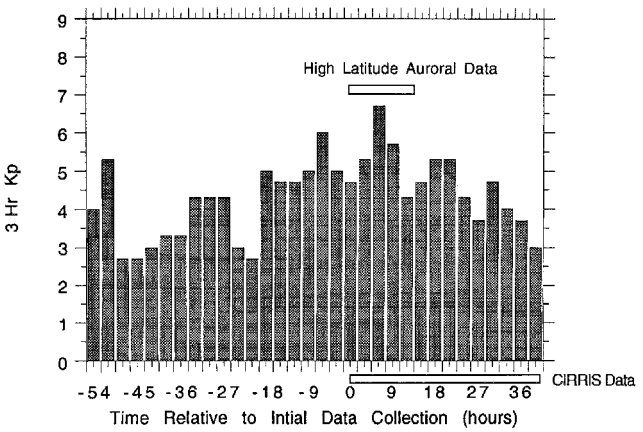

Fig. 2 Geomagnetic activity before and during the CIRRIS-1A observations.

The CIRRIS experiment was conducted during a major geomagnetic storm period. This facilitated the collection of a significant amount of data on moderate to bright aurora. Although this was not specifically planned, the shuttle launch was timed to take full advantage of such a chance event. This was accomplished by setting the launch time such that the tangent point of the line-of-sight intersected the midnight sector of the auroral oval during CIRRIS auroral observation modes. A record of the K_p history for the time period shortly before and during the CIRRIS mission is shown in Fig. 2.

The approach of this paper is to present a broad perspective of the results of this experiment. In the first part of the paper we present an overview of the sensor package and a brief discussion of the main sensor calibration and on-orbit operations and constraints. In the second part of the paper we present the data collection strategy and a summary of the scientific results and the significant findings made to date.

Overview of the CIRRIS-1A Instrumentation and Performance

Introduction

The CIRRIS experiment consisted of a moderate spectral resolution (~1.0 cm^{-1}) Michelson interferometer and a high-spatial resolution radiometer, which shared the collection optics of a cryogenically cooled (~12 K) high off-axis rejection IR telescope. An assembly of ancillary sensors, which included various photometers and cameras made up the remainder of the optical instrument package. This entire package of instruments was mounted on a two-axis gimbal system.

Figure 3 is an artist's view of the CIRRIS-1A instrumentation including the cryogenic dewar, the two-axis gimbal system, and the

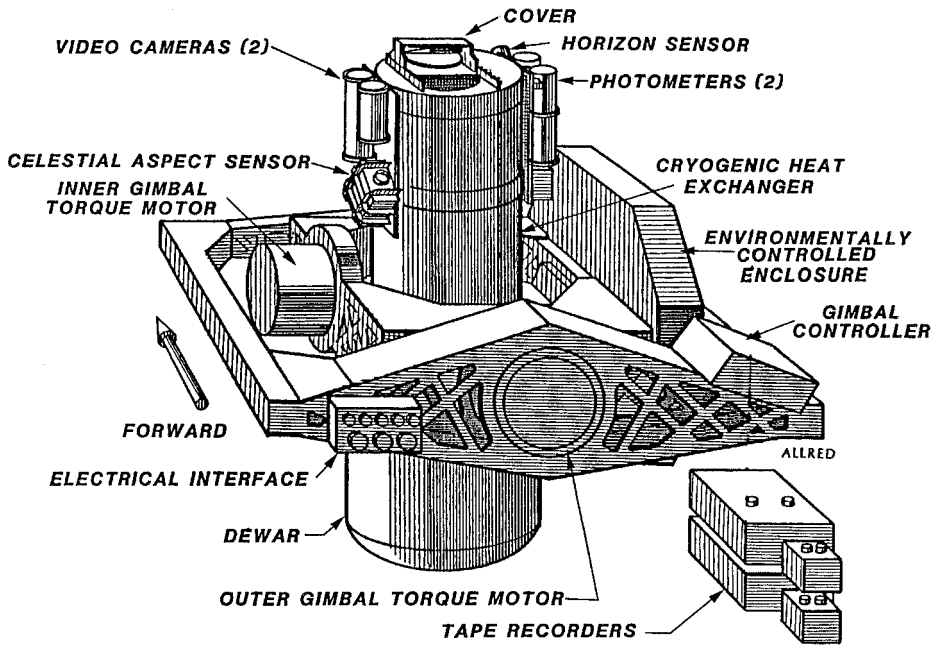

Fig. 3 Schematic of the CIRRIS-1A instrumentation package.

Table 1 CIRRIS-1A sensor specifications

Parameter	Interferometer	Radiometer
Detectors	5-Element Si:As IBC FPA	9-Element Si:As FPA 5-Element Si:Bi FPA
Spectral range/optical filters	2–25 μm, 8 selectable filters	2–25 μm, 7 selectable filters 1 Fixed filter at 2.7 μm
Spectral resolution	Theoretical: [full width at half maximum (FWHM)] 0.63 cm^{-1} unapodized 1.03 cm^{-1} with K-Bessel apod. Actual measured: (FWHM) 0.95 cm^{-1} unapodized	
Spectral accuracy	Better than $\pm$ 0.2 cm^{-1}	
Noise equivalent spectral radiance (NESR)	4×10^{-13} W $cm^{-2} \cdot sr^{-1} \cdot cm^{-1}$ at 700 cm^{-1} for D3-2	
NER		5×10^{-11} W $cm^{-2} \cdot sr^{-1}$ for D1-6
Dynamic range	A/D converter 6.5×10^4 Feedback resistor differences 3×10^2 Electronic gain 1×10^2 2 Bias levels 3×10^0 Ratio of detector areas 1.6×10^1 Total dynamic range (DR) 9.4×10^{10}	A/D converter 6.5×10^4 Feedback resistor differences 1×10^0 Electronic gain 1×10^2 3 Bias levels 1×10^2 Ratio of detector areas 2.4×10^1 Total DR 1.6×10^{10}
FOV (total)	0.93×1.5 deg	1.2×0.2 deg
Instantaneous FOV	10×10 mrad (D3-2)	0.5×3.0 mrad (FP1 and 2)
Spatial footprint at tangent point	14×14 km at 100 km tangent height (TH)	0.7×4.3 km at 100 km TH
Aperture	161 cm^2	182 cm^2
Chopper	——	Tuned fork at 84.6 Hz
Telescope off-axis leakage, NRER (11–13 μm band)	$1.0 - 2.0 \times 10^{-10}$ W $cm^{-2} \cdot sr^{-1}$	$0.5–2.0 \times 10^{-9}$ W $cm^{-2} \cdot sr^{-1}$
Calibration accuracy	less than $\pm$5-10%	$\sim \pm 5\%$
LOS determination accuracy	$\pm$ 1.0 mrad (nighttime) $\sim \pm$ 1.0–3.0 mrad (daytime)	
Tangent height accuracy at 100 km	$\pm$ 1.4 km (nighttime) $\sim \pm$ 1.4–4.3 km (daytime)	

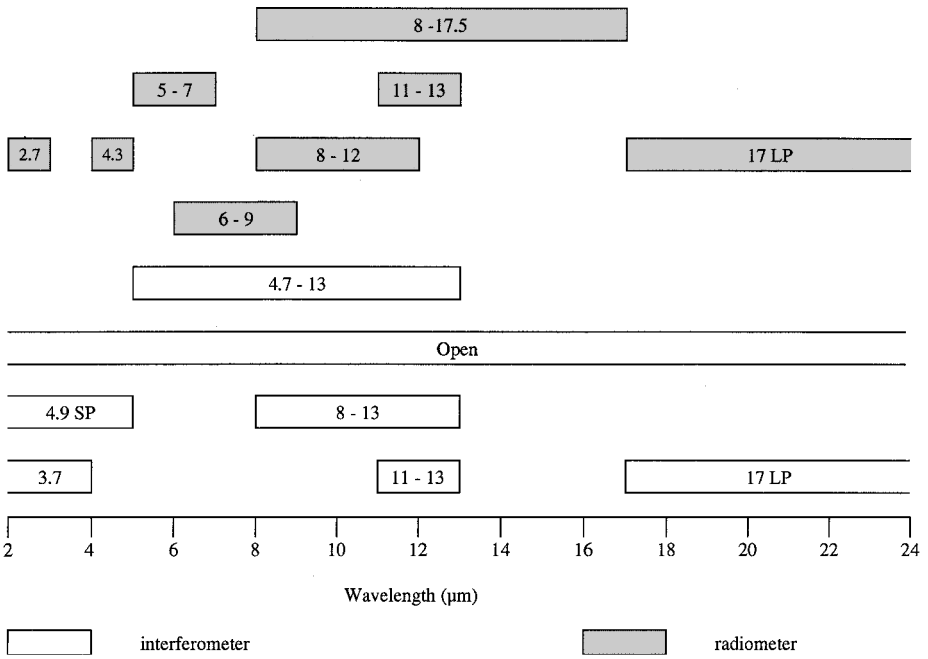

Fig. 4 Interferometer and radiometer filter passbands.

ancillary sensors. Most of the sensors and supporting instrumentation were developed and built by Utah State University, which also performed the instrument testing and calibration. The gimbal system was designed and built by Orbital Sciences Corporation. The experiment package was mounted on an experiment support structure, built by Lockheed–Martin, which was in turn mounted to the trunnion of the Space Shuttle *Discovery*. Brief descriptions of the instrumentation and experiment have been previously reported by Ahmadjian et al.[6,7] and Bartschi et al.[8,9] The CIRRIS 1A interferometer is similar to the SPIRIT interferometers flown on the SPIRIT I (Ref. 10) and SPIRIT II (Refs. 11–13) IR auroral rocket experiments and the SPIRIT III sensor flown on the MSX satellite.[14] A summary of the main sensor specification is given in Table 1. As indicated in Table 1, the CIRRIS-1A radiometer and interferometer each had a number of selectable optical filters. The passbands for these filters are shown in Fig. 4.

Telescope Off-Axis Rejection Assessment

One of the key elements in the success of the CIRRIS experiment was the excellent in-flight performance of the high rejection telescope. The primary function of the telescope was to collect energy for the interferometer and radiometer from atmospheric and celestial sources in the field of view (FOV) while substantially reducing and rejecting all sources of unwanted radiation. The two main sources of unwanted radiation are thermal self-emissions from the instrument and telescope and light scattered onto the detectors from off-axis sources such as the Earth and the lower atmosphere. The instrument's thermal emissions were effectively reduced by cryogenically cooling and maintaining the interferometer, radiometer, and telescope optics at a temperature of ~20 K for the entire CIRRIS mission. To reject contamination from off-axis radiation scattered into the FOV, both effective baffling and a very low-scatter primary mirror were employed. The radiation shade/baffle was designed to eliminate direct illumination of the primary mirror from sources beyond the 10-deg baffle angle, and a series of concentric photoetched knife edges of 0.001 in. radius minimized direct scattering from the baffles themselves. However, the most important element in determining the overall off-axis rejection capability is the scatter characteristics of the primary mirror because it alone must reject the direct off-axis illumination for angles between 10 deg and the interferometer FOV (1.2 × 1.5 deg). To achieve the design goal of an overall off-axis rejection of better than 10^{-10} μsr^{-1} at 2.5 deg from the edge of the FOV, it was determined that a bidirectional reflectance distribution function (BRDF) of 10^{-4} sr^{-1} was required for the primary mirror. Laboratory measurements of the primary and secondary telescope mirrors in their pristine condition confirmed that this design requirement (BRDF = 10^{-4} with a Θ^{-2} rolloff) had indeed been met. However, based on analysis of experimental data from other similar Earthlimb sensors,[15] there were serious concerns about whether this level could be maintained throughout the testing, calibration, integration, and launch phases of the program. Added to these concerns, there were special concerns regarding contamination of the telescope mirrors once the instrument cover was opened onorbit, due to expected high levels of gases and particulates surrounding the shuttle.

Preflight stray light analysis of the CIRRIS-1A telescope system predicted that the off-axis rejection performance would be primary-mirror scatter limited. As a result of these calculations, considerable time and effort was devoted to monitoring and maintaining the low-scatter characteristics of the telescope primary mirror throughout the rather lengthy 3-year preflight integration and test period. BRDF measurements on the primary mirror were made eight times during this period, including one made several months after the CIRRIS mission. The last measurement before launch indicated a relatively clean mirror with a BRDF value of 6×10^{-4} sr^{-1}. The CIRRIS primary mirror BRDF history was reviewed by Wheeler et al.[16] These authors[16,17] also presented a detailed discussion of the stringent preflight cleanliness procedures and summarized the onorbit operational constraints employed to avoid further (in-flight) mirror degradation from various known shuttle contamination sources.

The nonrejected Earth radiance (NRER) is a measure of an Earthlimb sensor's ability to reject off-axis radiation from the Earth (and the lower atmosphere) while viewing radiation from the upper atmosphere. Because this value is usually well above the detector noise level (NER), it generally sets the minimum background radiance level (atmospheric or zodiacal light) that can be measured by a sensor in a particular passband operating in an Earthlimb geometry. The definition of NRER used in this paper includes off-axis contributions from the lower atmosphere as well as those from the hard Earth. NRER can be measured at any wavelength, but is generally measured in the 11–13-μm window region where it is nearly always the limiting background at high tangent heights. Not only is this window region relatively free of atmospheric emissions, it is also near the peak of the Earthshine spectrum. The radiance vs altitude profiles in the 11–13-μm passband exhibited radiances that were nearly flat at tangent heights above about 100 km. These leakage radiance floors were well above the noise radiance floors for each detector and appeared to be characteristic of NRER. Furthermore, these profiles were generally consistent with model predictions of NRER that assumed a primary mirror BRDF that was only slightly worse than the preflight measured value of 6×10^{-4} sr^{-1}. However, the observed NRERs varied significantly from detector to detector for both the radiometer and interferometer. For the interferometer, the detectors that were closest to the center of optical axis (D3-4 and D3-2) exhibited the lowest NRER. Generally, the interferometer detectors exhibited less leakage than the radiometer detectors, although the best radiometer detector (D1-2) had an NRER that was comparable to the interferometer detectors. However, the worst radiometer detector (D1-1) had off-axis leakage that was about a factor of five higher. NRER values for the radiometer and interferometer in the 11–13 μm spectral region were presented by Wheeler et al.[16] and are also given in Table 1. The measured NRERs for the best detectors was approximately 1×10^{-10} $W/cm^2 sr$ in the 11–13 μm region for tangent heights above ~150 km. This is about a factor of 5–30 better than that achieved by previous Earthlimb measurements.[10,15,18,19]

Data Collection and In-Flight Operations

Operational Constraints

Great care was taken during and before the CIRRIS mission to avoid and control payload and sensor contamination levels. The CIRRIS-1A payload was assembled under carefully controlled conditions at Utah State University. Following integration into the shuttle cargo bay, the entire cargo bay section was carefully cleaned in the orbiter processing facility and then again on the launch pad just before launch. After launch, in the early part of the mission, all surfaces of the shuttle were subjected to an extended solar exposure period (bakeout) to accelerate the vehicle outgassing process. Next, the CIRRIS experiment was restricted by a number of operational constraints. The first of these constraints was to delay the start of CIRRIS measurements for a time (~1 day) sufficient to allow the initial contamination (mostly water trapped in the shuttle tiles) to decay to acceptable levels. Once the CIRRIS cover had been opened, the majority of the CIRRIS observations were performed in one of several relatively stable gravity-gradient (nose-to-Earth) modes with the sensors looking into the wake and with all of the thrusters inhibited. Other contaminating events, for example, shuttle water dumps, were also inhibited during CIRRIS observations. To further minimize in-flight contamination, cover-closed contamination cleanup periods were imposed during and immediately after each contaminating event. Many of these initial constraints were later relaxed as the mission progressed, and it became increasingly evident that overall contamination levels were not especially high. A summary of these in-flight operational constraints is given in Table 2.

Measurement Blocks

CIRRIS data were collected in a series of separate measurement periods called measurement blocks. Each block consisted of a number of individual measurement modes strung together in sequence. These measurement modes will be described briefly in the next

Table 2 Summary of CIRRIS operational constraints imposed during the STS-39 mission

Contaminating event	Action taken to avoid	Operational constraint	
Initial shuttle/tile outgasing	Delay initial cover opening, h[a]	23	(20)
Thruster firings	Allow a cleanup period after thruster firings, min[a]	15	(2)
Shuttle water dumps	Allow a cleanup period after water dumps, min[a]	90	(60)
Exposure to ram direction	Maintain a minimum angle between the sensor LOS and the velocity vector of the shuttle, deg	90	90
Exposure to direct sunlight	Maintain a minimum angle between the sensor LOS and the LOS to the sun, deg	85	85

[a]Time after event or launch: preflight or initial (late time or actual).

Table 3 Summary of the CIRRIS measurement blocks and their scientific objectives

	Nightglow			Dayglow			Sunset				Sunrise			
Block	Species	Band, μm	Type	Species	Band, μm	Type	Altitude, km	Species	Band, μm	Type	Altitude, km	Species	Band, μm	Type
PC 10 B initial airglow				Survey	4 SWIR[a]/ MWIR[b]	Spectral								
PC 11 A	Survey	Open	Spectral				100	Multiple	Open	Spectral	120	NO	5–13	Spectral
Open-filter, airglow	Survey	8–17	Spatial					CO_2	8–17	Spatial		NO	5–7	Spatial
PC 11 B	CO_2	4.9 SP[c]	Spectral	CO_2	4.9 SP	Spectral	100	Survey	Open	Spectral	100	Survey	Open	Spectral
MWIR airglow		4.1–4.5	Spatial		4.1–4.5	Spatial		CO_2	4.1–4.5	Spatial		CO_2	4.1–4.5	Spatial
PC 11 E				O_3	8–13	Spectral								
ozone airglow				O_3	8–12	Spatial								
PC 11 F	Wind B	11–13	Spectral	Wind B	11–13	Spectral	30	Wind B	11–13	Spectral	80	Wind B	11–13	Spectral
window B airglow	Wind B	11–13	Spatial	Wind B	11–13	Spatial		Wind B	11–13	Spatial		Wind B	11–13	Spatial
PC 11 G	H_2O	17 LP[d]	Spectral	H_2O	17 LP	Spectral	90	OH	3.7SP	Spectral	90	O_3	8–13	Spectral
window C airglow								O_3	8–12	Spatial		O_3	8–12	Spatial
PC 12A	Survey	4 LWIR[e]	Spectral	Survey	4 LWIR	Spectral	90	O_3	8–13	Spectral	60	Wind C	17 LP	Spectral
far-IR survey								O_3	8–12	Spatial		Wind C	17 LP	Spatial
PC 12B	Survey	4 SWIR/ MWIR	Spectral	Survey	4 SWIR/ MWIR	Spectral	70	——	5–13	Spectral	90	OH	3.7 SP	Spectral
near-IR survey								O_3	8–12	Spatial		O_3	8–12	Spatial
PC 13	Survey	7 SWIR–LWIR	Spatial	Survey	7 SWIR–LWIR	Spatial	75	OH	3.7 SP	Spectral	120	NO	5–13	Spectral
two-dimensional airglow								O_3	8–12	Spatial		NO	5–7	Spatial

[a]Short-wavelength IR. [b]Midwavelength IR. [c]Short pass. [d]Long pass. [e]Long-wavelength IR.

section. The measurement sequence for a typical block included a sunset terminator mode, followed by a nightglow staircase mode, followed by a sunrise terminator mode, and finally a dayglow staircase mode. A summary of the majority of the CIRRIS measurement blocks and their scientific objectives is shown in Table 3. Not included in this Table 3 are the auroral, horizontal stare, shuttle glow, celestial, and nadir-looking measurement blocks that provided additional data.

The optimum shuttle orientation for Earthlimb data collection is with the orbiter flying in a stable nose down gravity-gradient attitude. This is the most stable attitude with the thrusters inhibited. However, the small oscillations in pitch about this orientation tend to increase over a number of orbits. Therefore, to minimize these oscillations, it was decided that the orbiter would be retrimmed on every orbit. The retrim sequence consisted of a 15-min maneuver, a 5-min damping period, and then a 10-min wait period to allow for contamination from the vernier thruster firings to cleanup. Only after this sequence was completed, would the cover be reopened and measurements continued. This requirement allowed a maximum of approximately 1 h per orbit for CIRRIS observations.

Measurement Modes

A number of measurement modes were constructed to sample the atmosphere in a variety of different ways. These modes were grouped into several separate categories: staircase modes, raster scans, stare modes, and vertical sweep modes. Various combinations of these modes were put together to make up the numerous measurement blocks listed in Table 3.

The vertical staircase modes were the primary measurement modes for the collection of interferometer data from CIRRIS. These staircase modes sampled the atmosphere at discrete tangent heights, taking a combination of short, medium, and long scans at each step for a single interferometer filter position. The staircase was then repeated for each of the remaining interferometer filters. The stare modes were divided into two types: automated and interactive. The interactive stare modes were devised for collecting auroral spectra at high resolution. The payload specialists were free to use the joystick control to point the sensor at the brightest auroral features. Excellent auroral spectra were collected for various altitudes up to approximately 200 km, and it was in these data that the rotational bandheads in NO were first identified. These stare modes were also used for celestial calibrations. Very useful in-flight calibrations were obtained from measurements of α-Scorpio (Antares) and α-Bootes (see section on CIRRIS celestial observations). The automated stare modes were used for terminator crossing data collections, where constant tangent height stares were employed. The raster scans were devised

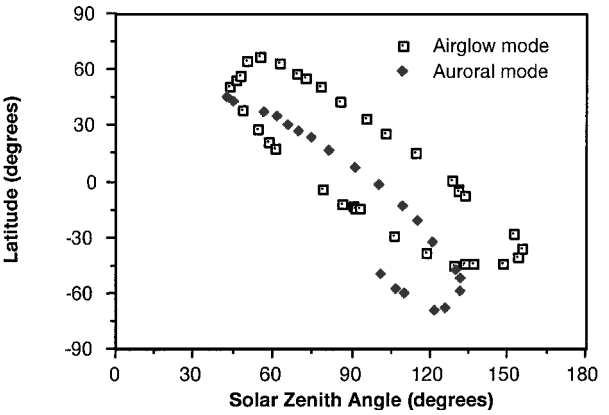

Fig. 5 Locations of the 100 kilometer tangent points of the LOS plotted in latitude vs SZA space.

to study the spatial structure in various bands. Finally, rapid vertical sweep scans were used to measure the radiance profiles for each of the seven radiometric filter bands.

Orbit-Imposed Constraints on the Data

The shuttle was launched from Cape Kennedy, Florida, into a 260-km circular orbit on 28 April 1991. A launch time of approximately 6:30 a.m. local time was chosen to have the line of sight (LOS) of the CIRRIS sensors intersect with the midnight sector of the southern auroral oval. The effect of this launch time was to restrict the CIRRIS airglow measurements to nighttime conditions in the southern hemisphere and daytime conditions in the northern hemisphere. The majority of the data collections were conducted in a nose down gravity-gradient mode in three orientations: gravity-gradient north, gravity-gradient south, and belly-to-ram. The gravity-gradient north orientation pointed the shuttle's cargo bay away from the sun and was used for about 75% of the CIRRIS measurements. Employing this shuttle attitude, in conjunction with the selected early morning launch time, dictated that most of the nighttime airglow observations occurred at midlatitudes in the southern hemisphere, whereas the dayglow observations occurred primarily at high latitudes in the northern hemisphere. The gravity-gradient south and belly-to-ram orientations were used for targeting aurora, which resulted in nighttime high-latitude observations in the southern hemisphere. The celestial observations required bay-to-space attitudes. Figure 5 summarizes the effect of the shuttle

attitude and orbit on the distribution of CIRRIS Earthlimb data. Figure 5 shows the orbit-limited distribution of CIRRIS Earthlimb observations as plotted in solar zenith angle (SZA) vs latitude space for the two primary measurement modes.

Sensor Calibration

The calibration of the CIRRIS primary sensor was performed in two phases. The first phase was the engineering evaluation. The engineering evaluation was performed before payload integration. This evaluation was used to verify that sensor performance met the mission requirements and established preliminary calibration coefficients. The second calibration phase was the postflight calibration. This calibration phase provided a full characterization of the primary sensor. This full characterization included the radiometric equation to convert sensor outputs into radiometric values and a radiometric model to transfer the measured radiometric values to the true scene flux.

Each calibration test performed was directed toward measurement of a specific radiometric parameter. These individual parameters make up the radiometric equation and model. They are classified into four distinct domains: spatial, spectral, temporal, and radiometric responsivity. For the CIRRIS primary sensor most parameters were characterized for each detector. The spectral and radiometric responsivity was further specified for every filter position for each detector. Collectively the parameters that characterize each of these domains comprised a complete calibration of the CIRRIS primary sensor. The results of this calibration are presented in the CIRRIS-1A postflight calibration report (published in two volumes).[20,21] Additional information from the coalignment procedures established the position of the radiometer focal planes with respect to the interferometer focal plane and the interferometer focal plane with respect to the interferometer field stop.

The CIRRIS-1A sensor contained a number of internal stimulators and calibration sources. These sources were used before and during the CIRRIS mission to monitor the performance of the interferometer and radiometer and also the condition of the low-scatter primary mirror. Several of the stimulators were positioned to reflect off of the back of the instrument aperture cover and were visible to both the interferometer and radiometer. Other stimulator sources were located near the radiometer focal plane arrays and were visible only to the radiometer. A blackbody source and an alignment source were visible only to the interferometer. The blackbody source was located at the entrance to the interferometer cube and was used to monitor the performance of the interferometer. These sources were also used to provide in-flight calibrations of the two main sensors.

Pointing/Tangent Height Determination and Accuracy

The accurate determination of the LOS pointing in terms of its closest approach to the Earth disk (tangent height) is crucial for the analysis of data taken by a spaceborne sensor viewing the Earthlimb. This is particularly true for stratospheric observations where the accuracy of derived volume mixing ratio (VMR) profiles are critically dependent on the accuracy of the tangent height determination. Therefore, it is important to discuss in some detail the data and methods used to determine the tangent heights and the uncertainties associated with these values. A more detailed discussion of these issues can be found in the paper by Bingham et al.[22]

The LOS of the CIRRIS-1A interferometer and radiometer detectors was determined using information from a number of onboard instruments in conjunction with pre- and postflight ground-based alignment measurements. The onboard instruments and sensors included a celestial aspect sensor (CAS), an IR horizon sensor (IHS), gimbal system optical encoders, and the orbiter gyros. The relative alignment of these various sensors will be discussed next.

Sensor Alignment

As mentioned, the pointing solutions for the CIRRIS LOS depended on the data from a number of separate instruments used as aspect sensors. As a result of this, the accuracy of the pointing solutions for the CIRRIS interferometer/radiometer LOS is critically dependent on having an accurate knowledge of the relative alignment of these various sensors to the main sensor LOS. The relative alignment of these various instruments and sensors was established with both preflight and postflight theodolite measurements of alignment offset angles in conjunction with several in-flight celestial measurements that were used for the purpose of in-flight alignment validation.

The most accurate pointing solutions were derived from the star field images obtained with the CAS camera. The processing of these data provided an LOS accuracy for the CAS of approximately ± 0.25 mrad. However, the CAS and the main sensors were offset by an angle of approximately 45 deg, and it was the uncertainty in determining this large offset angle that resulted in the largest uncertainty in the pointing solutions derived from this instrument. This offset angle was accurately measured both before and after the flight, but these measurements indicated that unacceptable movement ($\sim$2 mrad) of the CAS had occurred sometime between these two measurements. Planned star measurements with the IR radiometers occurred during a dedicated IR radiometer calibration mode (PC36A) of the star, Antares. These measurements were used to establish an initial in-flight alignment offset between the CAS and the main sensor's LOS. The star crossings selected for this purpose were those where only the orbiter motion caused the star to track across the detectors (horizontal crossings with no gimbal motion). In addition, a chance sighting of the star α-Centauri occurred during an auroral measurement mode near the end of orbit 20. The best in-flight pointing reference occurred when this star passed across the smallest radiometer detector (D1-8) with a FOV of 0.5×0.5 mrad. Fortunately, these two in-flight measurements agreed to better than ± 0.5 mrad. Because the relative alignments of the radiometer and interferometer detectors were very accurately established during calibration of the main sensor, this allowed for an accurate in-flight determination of the critical offset angle between the LOSs of the CAS and each of the five interferometer detectors.

Tangent Height Determination and Accuracy

As mentioned earlier, the most accurate pointing solutions were obtained from the processing of the CAS star field images. Overall, nearly 1000 images were processed to determine pointing solutions. Most of these images were for nighttime or twilight conditions. As a result, the tangent heights associated with the daytime observations are generally less accurate than those for the corresponding nighttime measurements. However, it should be remembered that, due to the orbit constraints of the STS-39 mission discussed eariler, daytime observations were limited primarily to the northern hemisphere and nighttime data were obtained primarily from the southern hemisphere. The accuracy of the LOS determinations for the daytime measurements is directly tied to the accuracy of the IHS on which the daytime pointing solutions are based. These solutions are inherently less accurate than the corresponding nighttime CAS-based solutions by about a factor of 2. The limitations and accuracy of the pointing solutions based on this sensor have been discussed elsewhere.[22]

Fortunately, IHS-based solutions were available for both day and nighttime conditions. This allowed for the direct comparison of the two primary pointing solutions for nighttime conditions. From these comparisons, an accurate assessment of the errors in the IHS-based pointing was obtained. Based on the results of these comparisons, we estimate that the accuracy of the final pointing solution for daytime (northern hemisphere) conditions to be between ± 1.0 and 3.0 mrad, whereas the LOS accuracy for the nighttime (southern hemisphere) data is better than ± 1.0 mrad for the entire CIRRIS mission.

It is highly desirable that the LOS uncertainties be significantly less than the vertical resolution of the measurements; for the nighttime data, this is the case for all of the interferometer detectors (which range from 1.6 to 10 mrad) and all but the two smallest radiometer detectors (which are 0.5 mrad). However, because of the larger uncertainties in the daytime observations, this criterion is not always met for the daytime data. This was especially problematic for measurements at low altitudes (in the stratosphere), where the vertical footprints are largest and the most useful data were collected using the two smallest interferometer detectors (due to saturation of the big detectors). Fortunately, the large central detector (D3-2) was the primary detector for most of the CIRRIS observations that have

Table 4 Vertical resolutions at selected tangent heights for the primary interferometer and radiometer detectors

Tangent height, km	Vertical footprint (resolution) at the tangent point, km[a]	
	ID3-2	RD1-1 → RD1-6
0	18.5	5.6
25	17.6	5.3
50	16.4	4.9
75	15.5	4.7
100	14.4	4.3
150	11.9	3.6
200	8.4	2.5

[a]Footprints for the other interferometer detectors can be obtained by multipling the D3-2 values 0.48, 0.21, 0.156, and 0.156 for D3-1, D3-3, D3-4, and D-3-5, respectively.

been reported to date. As a result, the pointing accuracy is considered to be adequate for all of the mesospheric and thermospheric measurements for both day and night conditions.

The cited LOS accuracies correspond to maximum tangent height uncertainties of 2.5–5.4 km for the 200–15-km-tangent-height range. These values should be compared to the vertical footprints given for the primary interferometer and radiometer detectors in Table 4.

Overview of CIRRIS-1A Data

Several brief overview articles that summarized the CIRRIS-1A experiment and preliminary results were presented[7–9,23] in the period immediately following the initial data analysis in early 1992. However, very few CIRRIS data were presented in these preliminary reports, and the final calibration and pointing data were as yet unavailable. In the intervening years, numerous detailed papers, on various specific observations have been published by many authors from analysis of the spectral and radiometric data obtained by CIRRIS. These papers will be referred to and discussed in subsequent sections of this paper. The following is the first comprehensive overview of the CIRRIS data.

The CIRRIS-1A database is a compilation of atmospheric emission spectra and radiometric profiles measured in a limb-viewing geometry. As a result, the detected radiance includes emissions from all along the atmospheric path in the LOS and thus covers a range of altitudes. The brightness of spectral features is affected by optical thickness considerations along the path and, thus, is not a measure of local volumetric radiances. Likewise, the measured tangent height profiles are not vertical altitude profiles and, thus, do not represent radiance vs altitude at one location on the Earth. The tangent points for a typical vertical scan are spread out along a slant path that covers a range of many hundreds of kilometers.

Interferometer Spectral Survey Summary

Open Filter Spectra

In this section we present an overview of the broadband infrared spectra obtained with the open-filter position for various altitudes from the stratosphere to the lower thermosphere for both day and nighttime conditions. Examples of day and night spectra for a number of tangent altitudes between 13 and 165 km are shown in Figs. 6 and 7, respectively. Although the arsenic doped silicon detectors are sensitive throughout the entire 2.5–25-μm region, the spectral response falls off rapidly on the short-wave side of 4 μm and beyond about 22 μm on the long-wavelength side. For this reason, the open-filter data are only presented for the 4–22-μm spectral region. Coadding is generally required to achieve adequate signal to noise outside of this region.

A significant problem evident in many of the open-filter spectra was the presence of harmonic distortion (ghost) features. These ghost features appeared in the spectra at levels that ranged from one to a few percent of the real spectral features and were caused by nonlinearities in the interferometer detectors. Second-order (and occasionally third-order) harmonic features were often seen in the open-filter data depending on the particular detector used and altitude observed. This problem was particularly severe for spectra with

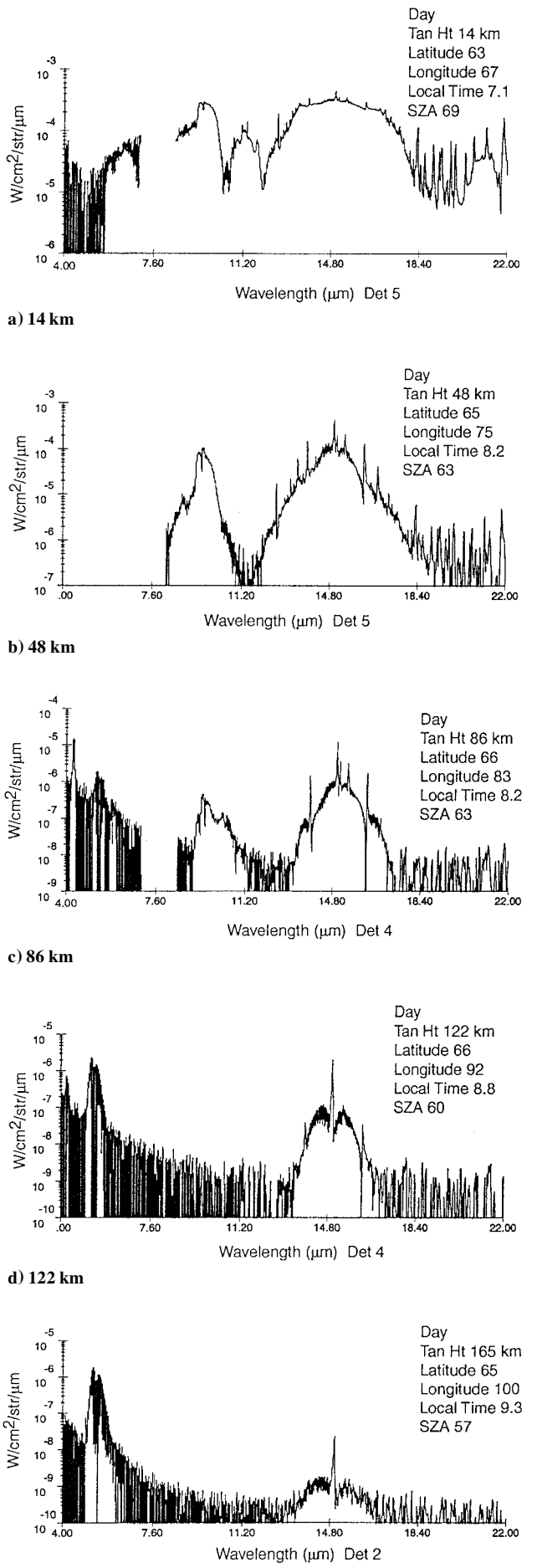

Fig. 6 Daytime spectra from the open filter for several altitudes.

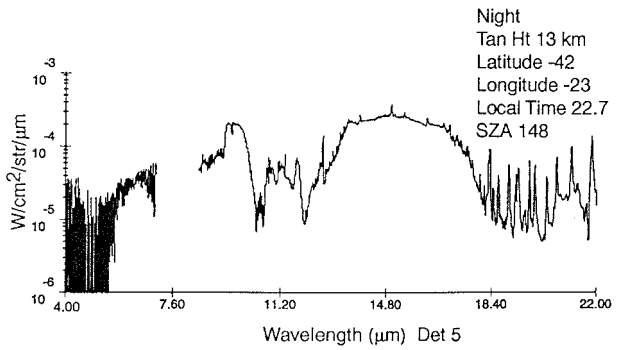

a) 13 km

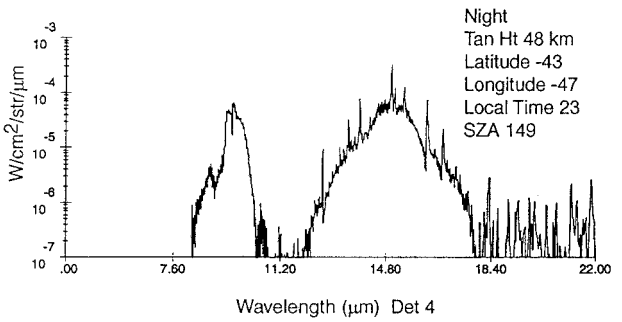

b) 48 km

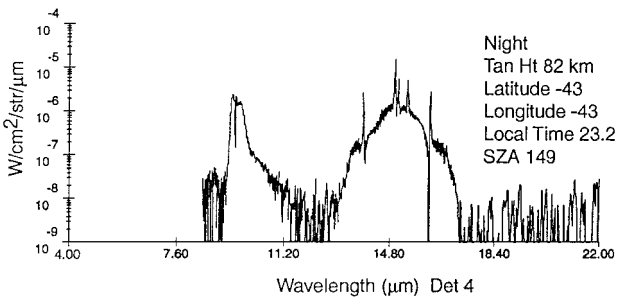

c) 82 km

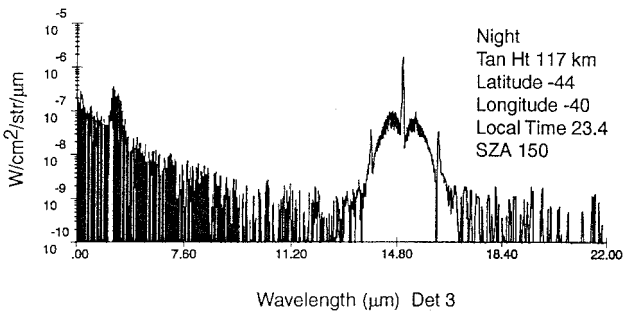

d) 122 km

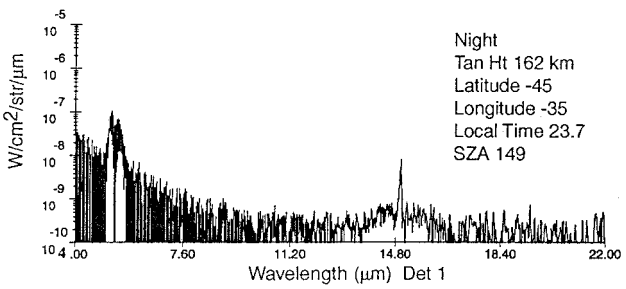

e) 162 km

Fig. 7 Nighttime spectra from the open filter at several altitudes.

tangent altitudes between ~40 and 85 km, where the 9.6-μm ozone and 15-μm CO_2 emissions are comparable in amplitude. In these cases, combination band ghost features (sum and difference bands) also appeared in the spectra, in addition to the normal harmonic distortion features. The presence of these artifacts in the open-filter interferometer data severely limited the usefulness of these spectra at tangent altitudes below ~120 km, where the data for wave numbers greater than 1700 cm^{-1} were essentially unusable. In a few extreme cases, five separate ghost features were observed in these open-filter spectra. These features were located at $2\sigma_1$, $3\sigma_1$, $2\sigma_2$, $\sigma_2 - \sigma_1$, and $\sigma_2 + \sigma_1$, where $\sigma_1 = 667$ cm^{-1} and $\sigma_2 = 1043$ cm^{-1} are the wave numbers of the $CO_2(\nu_2)$ and the $O_3(\nu_3)$ bands, respectively. In cases where these anomalous features occurred, they have been eliminated from the spectra and appear as regions of no data.

Stratosphere (14 kilometers). The dominant emission feature in the CIRRIS open-filter spectra in the lower stratosphere near the tropopause is the broad 15-μm CO_2 band system. The ν_2 ozone emission feature at 9.6 μm is also very prominent in these spectra, particularly in the nighttime data (see Fig. 7a). Between the strong ozone and CO_2 features is a region that contains several important molecular emissions, including CFC-12 (ν_8 at 10.9 μm), HNO_3 (ν_5 at 11.4 μm), CFC-11 (ν_4 at 11.8 μm), and CCl_4 (ν_3 at 12.5 μm). Vibrational and pure rotational emissions from water at 6.3 μm (ν_2) and 18–22 μm, respectively, are also present in these spectra.

Typical daytime spectra in the lower stratosphere are very similar to the nighttime spectra, except the emissions are about 30% higher. The integrated radiance from 4 to 22 μm is about 1.4×10^{-3} W/cm^2 · sr for the nighttime spectra in Fig. 7a, whereas for the daytime case (Fig. 6a) it is 1.9×10^{-3} W/cm^2 · sr. This may be due to warmer temperatures affecting the emissions and solar scatter contributions from water at the short wavelengths. Harmonic distortion (artifact) features that occur near 7.5 μm in both day and nighttime spectra have been removed from these data. These features are due to the first harmonic of the 15-μm CO_2 band.

Lower mesosphere (50 kilometers). Spectra in the lower mesosphere near 50 km (Figs. 6b and 7b) are dominated by the ozone (9.6 μm) and CO_2 (15 μm) features that are of nearly equal radiance. The greenhouse gas emissions in the 10.5–12.5-μm region that were so evident in the stratospheric spectra are greatly diminished. Vibrational and rotational emissions from water in the 6.3- and 17–22-μm regions, respectively, remain as significant features in the spectra at this altitude, and a second strong CO_2 emission feature (the ν_3 band) is now clearly evident in the 4.3-μm region. There is little or no difference between the day and nighttime spectra in this altitude range. Artifact features that occur near 7.5 and 5.8 μm have been removed from both the daytime and nighttime spectra. The ghost feature at ~5.8 μm (1710 cm^{-1}) is due to the sum of the 15-μm (667-cm^{-1}) and 9.6-μm (1043-cm^{-1}) bands.

Mesopause region (85 kilometers). Typical day and nighttime open-filter spectra in the mesopause region near 85 km are shown in Figs. 6c and 7c, respectively. These spectra continue to be dominated by the strong ozone and CO_2 emission features that also dominated the spectra at lower altitudes. The daytime spectra show six prominent features. In addition to the CO_2 and O_3 features at 15 and 9.6 μm, respectively, that appear in the nighttime spectrum, there are also strong emissions features from solar-pumped vibrationally excited CO_2 at 4.3 μm, from NO ($\Delta v = 1$) at 5.3 μm, and from the two CO_2 laser bands at 9.4 and 10.4 μm. The 9.6-μm ozone peak is significantly weaker in the daytime spectra than in the corresponding nighttime cases due to photodissociation of O_3 during the day. The 15-μm CO_2 emission is unchanged from day to night, as is also the case for the rotationally excited water vapor emissions in the 17–22-μm region. We have again removed artifact features that occur near 7.5 μm (day and night) and 5.8 μm (nighttime only) from these spectra.

Lower thermosphere (120 kilometers). Typical day and night open-filter spectra in the lower thermosphere are shown in Figs. 6d and 7d, respectively. In these spectra, which were obtained at ~120 km, the 9.6-μm ozone feature has vanished, and only two major emission features remain. These features are the NO fundamental band emission at 5.3 μm and the CO_2 (ν_2) band at 15 μm.

The band-integratedlimb radiances of these two features are roughly equivalent at night. The 4.3-μm CO_2 (ν_3) emission also appears as a narrow feature that is just barely detectable above the instrument noise level in the nighttime case. In the daytime spectra, the 4.3-μm CO_2 and the 5.3-μm NO emissions are enhanced over the nighttime case by about a factor of 3 and 5, respectively.

Lower thermosphere (160 kilometers). Typical day and nighttime interferometer spectra taken with the open filter in the lower thermosphere near 160 km are shown in Figs. 6e and 7e, respectively. The 5.3-μm NO fundamental band emission is the dominant feature in the nighttime spectra for tangent altitudes above about 160 km. The 15-μm CO_2 emission remains a prominent feature in these spectra, but it no longer dominates the spectrum as it did at lower altitudes. The 5.3-μm NO emission feature also dominates the daytime spectra at these altitudes. However, in these spectra, this emission is more than an order of magnitude brighter than the corresponding nighttime emission. This is at least partially because the daytime data were collected at a higher latitude (65°) than the nighttime data (45°). The daytime 15-μm CO_2 emission is also larger (by about a factor of 2) than for the nighttime case.

Interferometer Spectra from Selected Bandpasses

Spectra in the 3–4.9-micrometer passband (2040–3333 cm^{-1}). The emitters in this region are CO_2, NO^+, CO, O_3, OH, and H_2O. The CO_2 (ν_2) emission at 4.3 μm was observed throughout the lower atmosphere and mesosphere. Emissions from the NO^+ fundamental band were observed primarily in the daytime and the aurorally disturbed lower thermosphere. Using these spectra, we were able to differentiate between structure due to CO_2 and NO^+ in various altitude regions. Both of these emissions are enhanced in aurora. The NO^+ is observed mostly in the lower thermosphere. Below 100 km, the emission in this passband is almost exclusively due to CO_2, whereas above 100 km, the emission is from a combination of CO_2 and NO^+, with NO^+ dropping off more slowly than CO_2. There is significant diurnal variation in the emission from CO_2 due to solar fluorescence during the day. CIRRIS-1A spectra in the 2050–2200 cm^{-1} (4.55–4.88-μm) region near the mesopause was successfully modeled by Dodd et al.[24] as a superposition of emissions from O_3, OH, and CO. The following radiators were identified: O_3 ($\nu_1 + \nu_3$) at 2111 cm^{-1}, O_3 ($\nu_1 + \nu_2 + \nu_3 - \nu_2$) at 2084 cm^{-1}, OH (9–8) band at 2236 cm^{-1}, the fundamental bands of $^{12}C^{16}O$, and its two most abundant isotopes $C^{13}O^{16}$ and $C^{12}O^{18}$. Several examples of spectra obtained with the 4.9-μm short pass filter are shown in Fig. 8.

Spectra in the 4.7–13-micrometer passband (770–2080 cm^{-1}). The emitters in this region are CO, NO, and H_2O. Spectra from nitric oxide for day and night midlatitude conditions are shown in Fig. 9. The NO fundamental (1-0) emission at 5.3 μm dominates this passband above ~110 km and exhibits a strong diurnal variation. Results of the spectral analysis of the 5.3-μm region are summarized in a later section. In the daytime spectra, the peak of the P-branch of

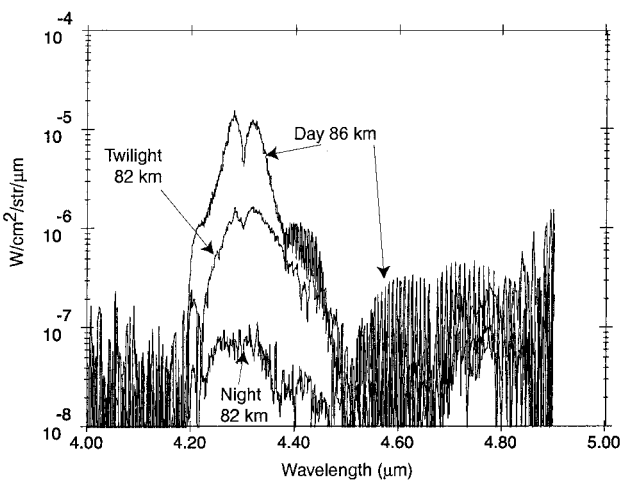

Fig. 8 Sample spectra from the 4.9-μm short pass filter in the mesopause region for day, night, and twilight conditions.

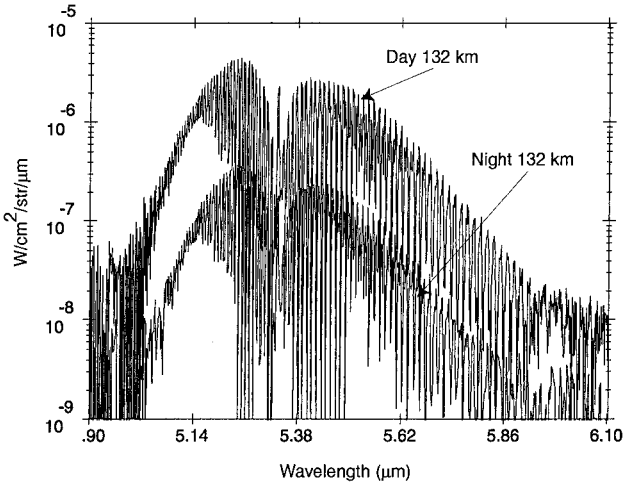

Fig. 9 Two midlatitude spectra for NO for day vs night conditions.

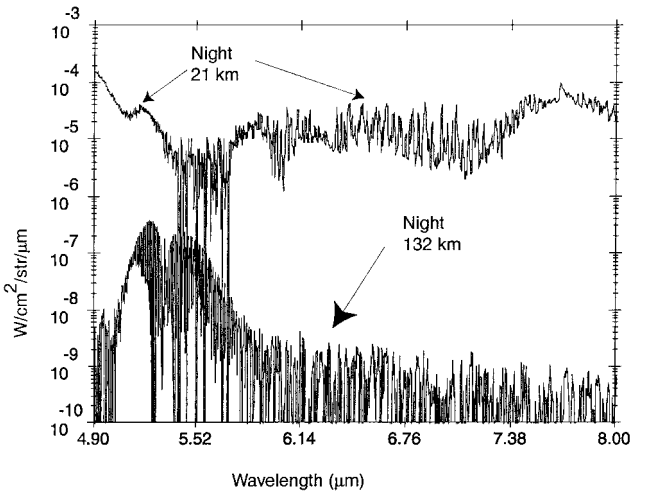

Fig. 10 Spectra from the 4.9–8 μm region from the stratosphere (21 km) and lower thermosphere (132 km).

the thermal distribution (centered around 5.42 μm) of spin $\frac{1}{2}$ can be distinguished from a second thermal distribution of spin $\frac{3}{2}$, which peaks around 5.5 μm. In Fig. 10, we compare nighttime spectra in the 4.9–8.0-μm region for two different tangent heights. In the stratosphere, the spectrum is dominated by CO (4.7 μm) and the water vapor continuum, including the 6.3-μm H_2O vibrational band. The band feature at 7.7 μm is due to methane. In the lower thermosphere, the only emission is due to the NO fundamental band at 5.3 μm.

Spectra in the 8–13-micrometer passband (775–1250 cm^{-1}). The emitters in this region are O_3, CO_2, the CFCs, and HNO_3. The ozone spectrum is one of the most complex systems in the IR region. In Fig. 11, we show several examples of spectra in this passband region taken at different altitudes for nighttime conditions. The spectra in this passband are highly dependent on the altitude of the observation. In the lower atmosphere, there is little diurnal variation, but as we examine higher altitude data, diurnal variations are much more dramatic. In Fig. 12, the spectra for day and night conditions are compared for a tangent altitude of about 72 km. Note that the O_3 (ν_2) peak emission is comparable for both day and nighttime conditions. However, additional emission features are apparent on both sides of the O_3 peak in the daytime spectra. These daytime features are the CO_2 laser lines at 9.4 and 10.4 μm. Pure rotational emissions from vibrationally and rotationally excited OH are easily discernible in the nighttime spectrum between 10 and 12 μm. At higher altitudes, near 85 km, there is a more pronounced diurnal variation due to dissociation of O_3 in daytime.

Spectra in the 11–13-micrometer passband (770–910 cm^{-1}). The 11–13-μm passband is often thought to be a window region, but

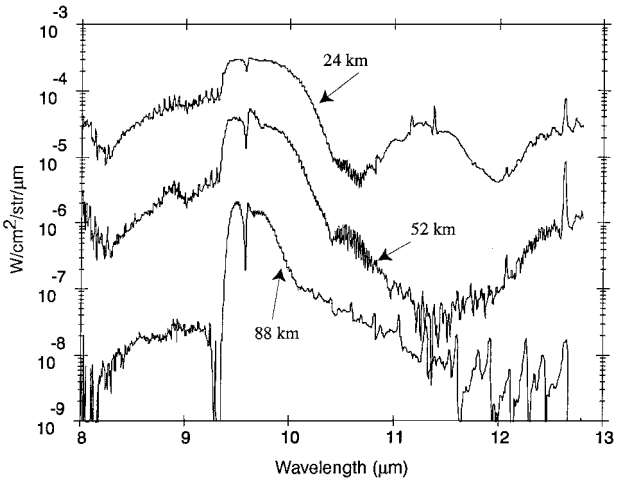

Fig. 11 Nighttime spectra from the 8–12-μm filter for three different altitudes.

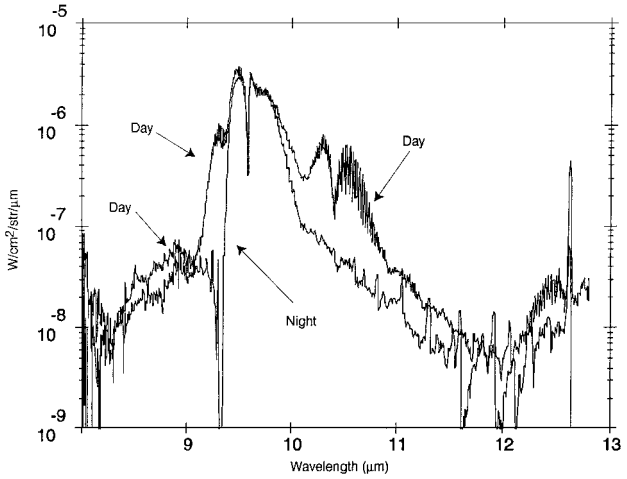

Fig. 12 Examples of daytime and nighttime spectra in the 8–12-μm region for an altitude of 72 km.

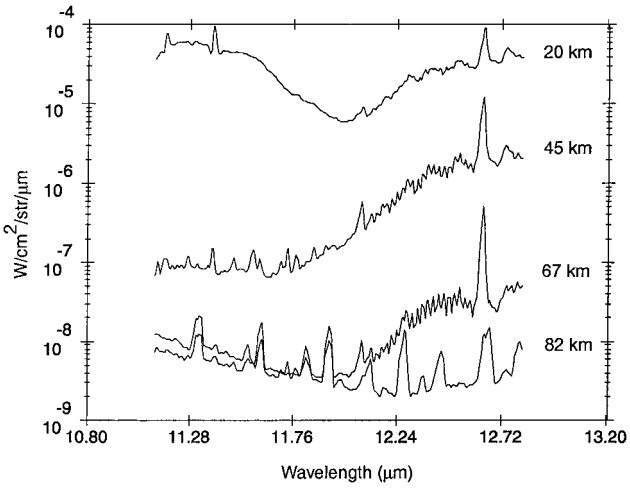

Fig. 13 Nighttime spectra in the 11–13-μm region at 20, 45, 67, and 82 km.

significant emissions were discovered in this window from high-N transitions of pure rotational OH (Refs. 25 and 26), as well as from CO_2, and several stratospheric trace gasses. Several typical nighttime spectra for various tangent altitudes are shown in Fig. 13. Note the OH pure rotational (high-N) emission lines in the 67- and 82-km spectra. Note also the incursion of the strong feature at 12.6 μm in the spectra below about 70 km. This is a satellite band of the strong 15-μm CO_2 ν_2 band system. This feature is easily discernible in the

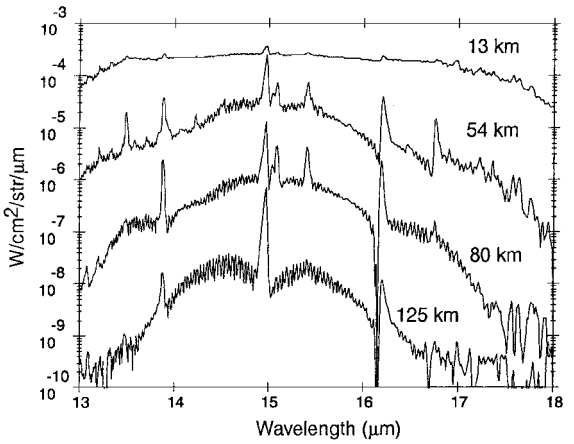

Fig. 14 Quiescent nighttime spectra of the CO_2 (ν_2) band system at 13, 54, 80, and 125 km.

daytime spectra up to about 100 km but is partially masked in the nighttime spectra at altitudes above 70 km by the presence of high-N (N = 24–33) pure rotational emissions from OH. At 20 km, emissions are primarily from nitric acid (11.3 μm) and CO_2 (12.6 μm).

Spectra in the 13–18-micrometer region (550–770 cm^{-1}). There was no interferometer (or radiometer) filter that isolated the 13–18-μm region of the spectrum; therefore, it was necessary to use the open filter data to analyze this part of the LWIR region. Typical nighttime spectra in this region for several tangent altitudes are shown in Fig. 14. The emitters in this spectral region are CO_2, H_2O, and O_3. The 15-μm CO_2 (ν_2) emission dominates the region, from the ground all the way up to 200 km, where the Q-branch could still be observed above the interferometer noise level. The O_3 (ν_2) emission is hidden beneath the R-branch of the 15-μm CO_2 (ν_2) band. Its contribution to the overall emission is thought to be relatively minor compared to CO_2 (about 1% of the 15-μm emission near the O_3 emission peak at 85 km). The variation in optical thickness with altitude and the constant mixing ratio of CO_2 in this band enable the user to derive temperature as a function of altitude. Emissions from H_2O occur throughout this region. The 15-μm CO_2 626 band system was examined for variations in relative spectral contributions to the total integrated 15-μm band emission. It was determined that emission enhancements related to geophysical conditions were the result of equal contributions across the entire band system, that is, the spectra could be overlaid except for a constant scale factor. These observations should be considered in conjunction with the results from the EXCEDE III experiment,[27] where the atmosphere was artificially dosed with a large flux of highly energetic electrons. Although this flux level was high enough to induce very high vibrational/rotational transitions in NO (higher than those observed in CIRRIS), no enhancements were observed in the 15-μm CO_2 emission. Based on the EXCEDE observations, it can be argued that the 15-μm enhancements observed by CIRRIS are probably not due to particle precipitation, but rather to increased CO_2 concentrations. Temperature retrievals above 100 km based on ratios of spectral lines in the P- and R-branches of the 626 band system were attempted using the method of Zachor and Sharma,[28] but were not successful. This may have been due to a lack of sufficient signal to noise and/or spectral resolution.

Spectra in the 17–25-micrometer passband (400–590 cm^{-1}). Observations in this region have been examined between about 20 and 120 km. The emission in this region up to about 80-km tangent altitude is dominated by pure rotational H_2O, which is characterized by numerous randomly spaced lines that belong to the P-branch of several subbands in the ground state. Emissions from CO_2 (544 cm^{-1}) and high-N (N = 13–17) pure rotational lines of OH also contribute to the spectra in this region. The daytime spectra are similar to the nighttime spectra except for the absence of OH, whose population is greatly reduced in the daytime. Nighttime spectra for various tangent altitudes are shown in Fig. 15. CIRRIS spectra in this region have been compared with the SHARC model[29–31] for both

day and night conditions with excellent agreement for the strong H_2O lines. At altitude above 80 km, emission from collisionally excited shuttle outgassed water vapor begins to contribute to the rotational water spectrum, and above 100 km the emission is due solely to this shuttle-induced water vapor contamination.[30,32]

Summary of Radiometer Broadband Emission Survey

In this section we present a sample of limb radiance vs altitude profiles for various CIRRIS-1A radiometric filter passbands. The diurnal variation of the limb emission is shown for each band. Note that the daytime profiles were generally obtained at high latitudes, and so there remains the possibility that these data are influenced by particle precipitation and Joule heating effects in the lower thermosphere. In addition, the daytime observations at high latitudes generally correspond to significantly lower SZAs than the daytime data for low- to midlatitudes, thus further complicating the analysis.

Significant diurnal and latitudinal variations were observed in a number of the filter bands. However, it was difficult to compare radiometer profiles at high altitudes (above 100 km) due to low signal to noise. Attempts to average the data at high altitudes were complicated by the presence of high-intensity outliers caused by transients resulting from within the signal processing system and also from gamma particle hits. These large transients heavily weighted the mean values resulting in artificially high (false) values for the mean radiances. These spurious data points were eliminated using straight-line demarcations separating them from the real data. The data were then sorted into 2-km altitude bins, with the mean and standard deviation determined for each bin. Figure 16 shows an example of a processed profile superimposed on the raw data. The average NER for this filter passband is 1.8×10^{-9} W/cm$^2 \cdot$ sr.

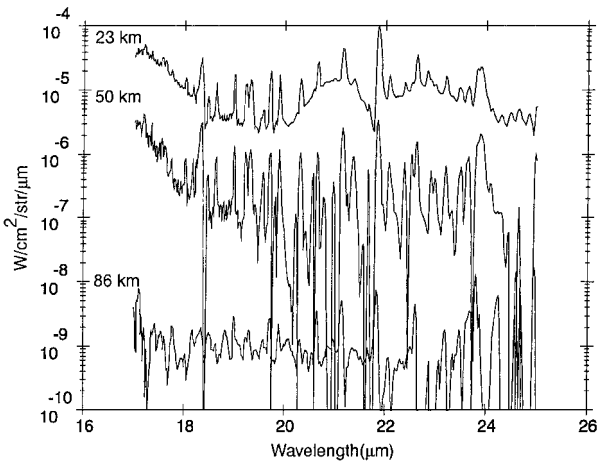

Fig. 15 Examples of nighttime spectra in the pure rotational water band region at 23, 50, and 86 km.

Radiometer Focal Plane 2 Data, 2.5–3.4-Micrometer Passband (2940–3985 cm^{-1})

Emissions in the 2.5–3.4 μm region are due to OH, CO_2, NO, H_2O, and aerosol scattering. Data were collected in this bandpass continuously throughout the CIRRIS experiment. The most prominent emission in this bandpass is due to the Meinel bands of the OH airglow emission, which peaks near 85 km. The fundamental band sequence extends from ~3600 to 2200 cm^{-1}, but only the first four transitions (4-3–1-0) fall within this optical passband. This Meinel band emission is brightest at night, due to production of vibrationally excited OH in the exothermic reaction of $H + O_3$, and diminishes during the day due to chemical recombination processes. Variations in the 2.7-μm OH emission are also caused by gravity waves that can introduce structure into the OH layer. Several typical profiles are shown in Fig. 17. Note the similarity in behavior between the nighttime low- and midlatitude profiles. The OH peak emission near 85 km is evident in the nighttime profiles. The daytime enhancement at lower altitudes (below 75 km) is due to solar pumped CO_2 and aerosol scattering. At high altitudes, there can be significant emission from the NO ($\Delta v = 2$) overtone band near 2.7 μm, which is an indication of chemical production of NO. The average NER for this filter passband is 1.8×10^{-9} W/cm$^2 \cdot$ sr.

The nighttime 2.7-μm profiles were examined for latitudinal and SZA dependencies. No significant relationship was found between peak radiance and latitude, or SZA. However, significant dependencies were found between the peak altitude and SZA and between the peak altitude and latitude (around local midnight). Unfortunately, latitude and SZA are not independent parameters in the CIRRIS

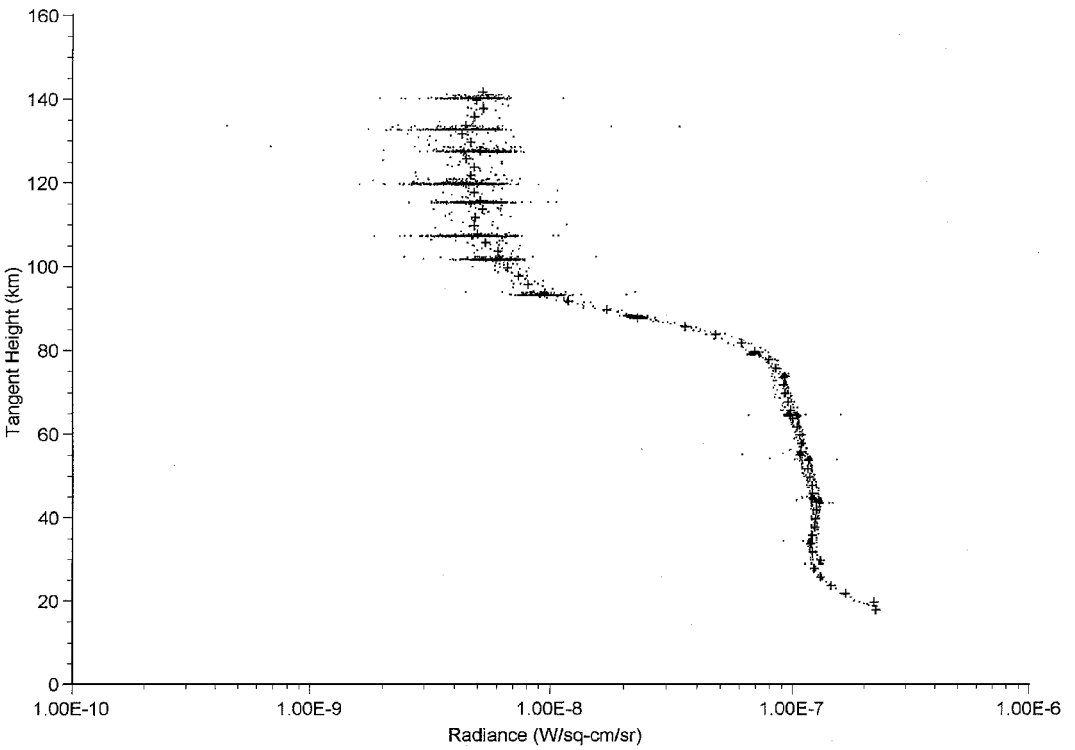

Fig. 16 Typical 2.7-μm (2.5–3.4-μm) profile for high-latitude daytime conditions showing the raw radiometric (FP2) data superimposed with the fitted profile (crosses) described in the text.

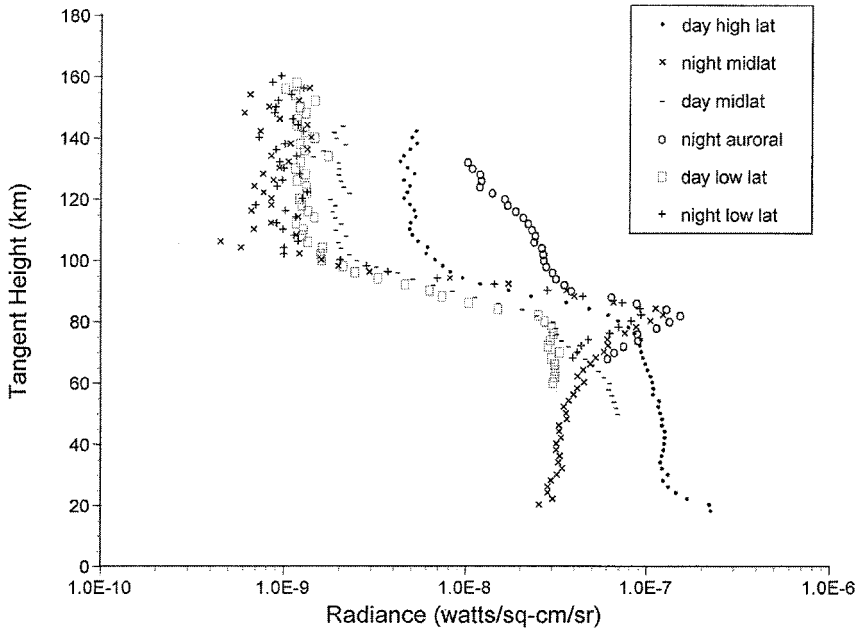

Fig. 17 Examples of typical 2.7-μm emission profiles for various observing conditions.

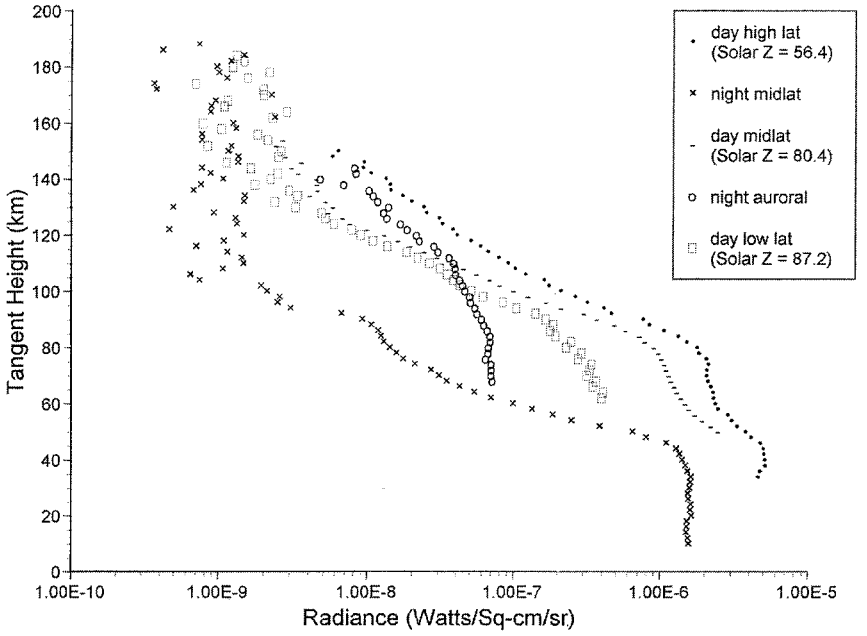

Fig. 18 Radiometer profiles for various conditions in the 4.1–4.5-μm passband.

database, and, therefore, it is difficult to determine whether the peak altitude was dependent on SZA, latitude, or a combination of the two. Modeling studies[33] of OH suggest a dependency on SZA that is generally consistent with the CIRRIS observations.

Radiometer Filter 1 Data, 4.1–4.5-Micrometer Passband (2210–2450 cm^{-1})

The main emitters in the 4.3-μm region are CO_2 (ν_3) and NO^+. Emissions in the 4.3-μm passband from CO_2 (ν_3) and NO^+ were observed for both day and nighttime conditions but are up to 60 times brighter in the daytime. These emissions are also enhanced in aurora. Several typical profiles are shown in Fig. 18. The average NER for this filter passband is 1.3×10^{-9} W/cm^2 · sr. Below 100 km, the emission is primarily due to CO_2, whereas above 100 km, the emission results from a combination of CO_2 and NO^+. The bump in the profile near the mesopause at night was determined to be the result of the 9-8 and 8-7 transitions of the OH ($\Delta v = 1$) fundamental band sequence, which emit throughout the 4.3-μm passband region. The daytime enhancements with SZA are due to CO_2 solar fluorescence. At altitudes above about 140 km, the emission is due primarily to NO^+.

Radiometer Filter 2 Data, 4.9–7.1-Micrometer Passband (1405–2060 cm^{-1})

The emitters in this region are CO, NO, and H_2O. Several typical profiles are shown in Fig. 19. The average NER for this filter passband is 5.9×10^{-10} W/cm^2 · sr. In the lower thermosphere this bandpass is dominated by the 5.3-μm NO fundamental band emission. The emission was observed from about 60 km up to shuttle altitudes of about 260 km. The variability of the 5.3-μm emission in the lower thermosphere is described by Wise et al.[34] The peak radiance of the 5.3-μm NO emission was found to vary between 105 and 140 km. Radiance vs tangent height profiles are shown for various atmospheric conditions in Fig. 19.

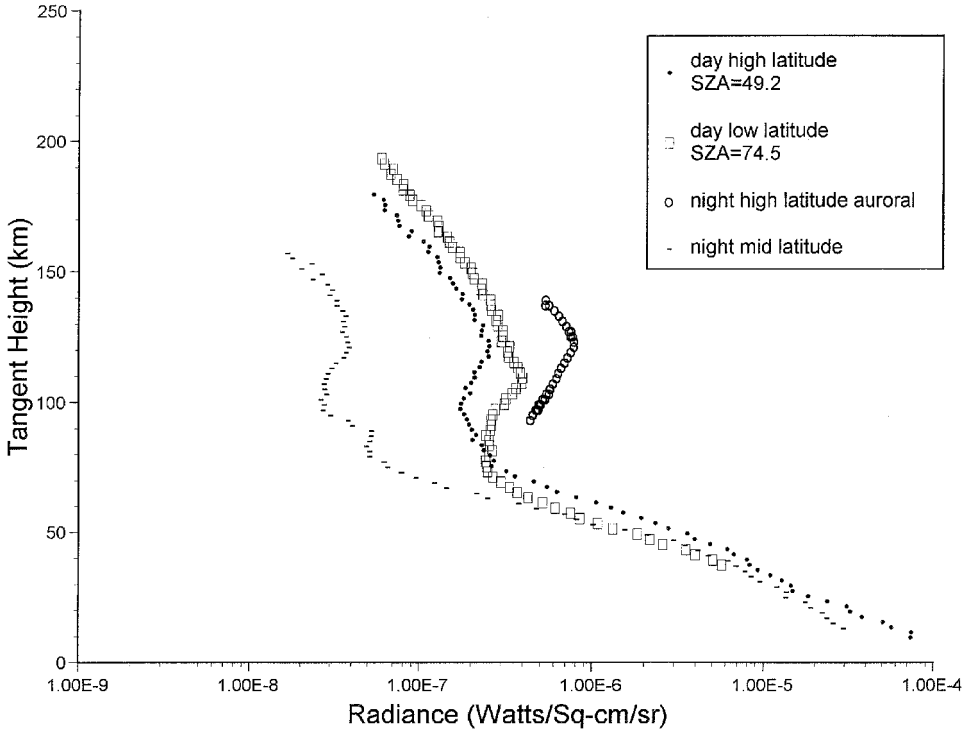

Fig. 19 Radiometric profiles for the 4.9–7.1-μm passband.

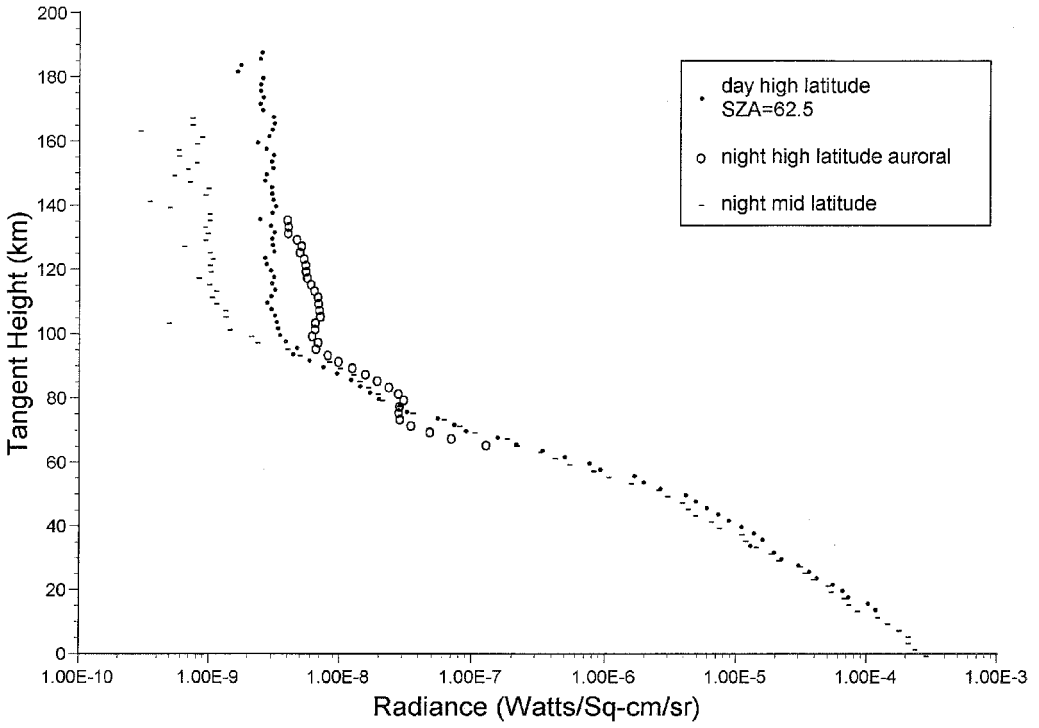

Fig. 20 Radiometric tangent height profiles in the 6–9-μm passband.

In many of the nighttime profiles, a bump can be seen around 85 km near the mesopause. This may be due to a temperature inversion. Between 70 and 95 km, emission from the fundamental band of CO makes a significant contribution to the total radiance observed in this passband. Below 70 km, the passband is dominated by emission from vibrationally excited H_2O at 6.3 μm.

Radiometer Filter 3 Data, 6–9-Micrometer Passband (1115–1690 cm^{-1})

The only significant emitters in this passband are NO and H_2O. Above about 80 km, this bandpass is generally considered to be a window region. However, P-branch emissions from the rotationally nonthermal component of NO (Refs. 35–37) are present throughout the 6–9 μm passband for both day and nighttime conditions. These nonthermal emissions vary with both local time and latitude and will be described in more detail in a future paper. The average NER for this filter passband is 4.2×10^{-10} W/cm^2 · sr. In the lower atmosphere and the mesosphere, the emission in this passband is dominated by the 6.3-μm water band and falls off very rapidly with altitude. For aurora and daytime conditions, the emission persists well above 100 km due to the rotationally hot component of the NO emission. Typical profiles are shown in Fig. 20.

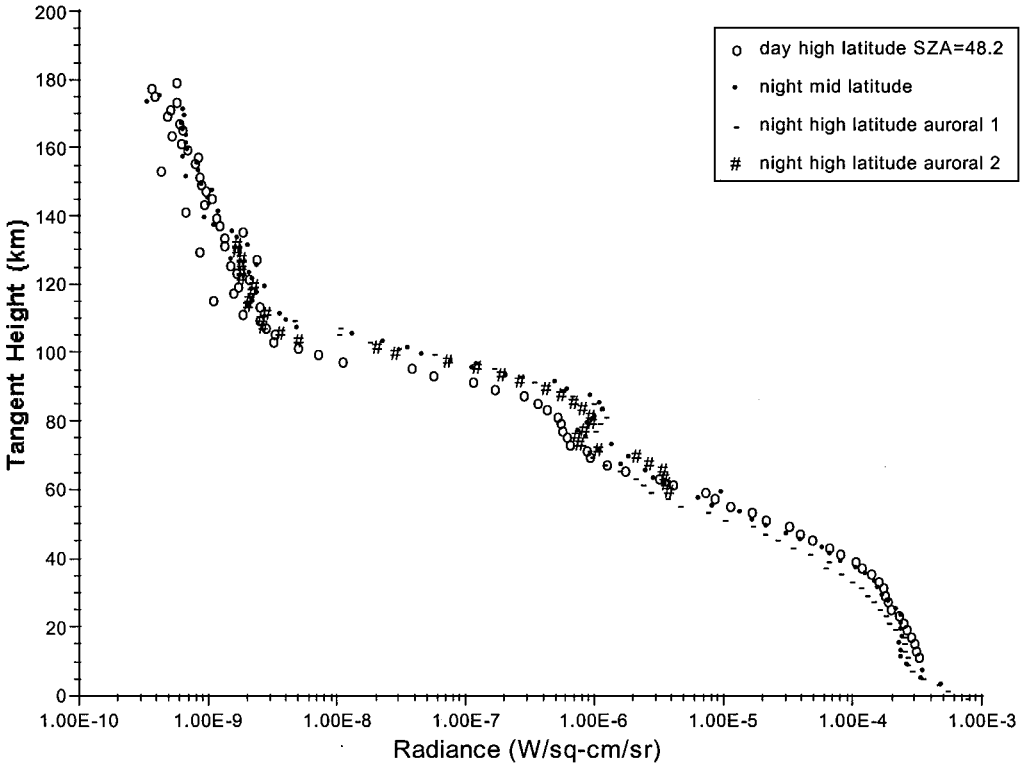

Fig. 21 Radiometric profiles in the 8–12-μm passband.

Radiometer Filter 7 Data, 8–12-Micrometer Passband (835–1250 cm^{-1})

Emission in the 8–12-μm passband is dominated by the ν_3 band of ozone at 9.6 μm. Emission from the ν_1 band of ozone at 9.1 μm is weaker than the ν_3 band by more than an order of magnitude and, thus, makes only a small contribution to the total radiance measured in this passband. In the daytime, between about 60 and 100 km emissions from the two solar-pumped CO_2 laser bands at 9.4 and 10.4 μm are significant contributors to the overall radiance in this passband. Above 105 km, the radiances are consistent with predictions for NRER due to telescope off-axis leakage. The O_3 (ν_3) emission peaks at about 85 km and diminishes rapidly with increasing altitude thereafter. Daytime radiances exceed the nighttime values up to about 60–65 km. At higher altitudes, depletion of ozone in the daytime causes the D/N ratio to fall below 1. Above 100 km, the nighttime radiances exceed the daytime values by about an order of magnitude. Variations are most notable at 85 km, where the secondary peak in the ozone concentration diminishes in the daytime due to solar photodissociation. The average NER for this filter passband is 2.2×10^{-10} W/cm^2 · sr. Typical profiles are shown in Fig. 21.

Radiometer Filter 0 Data, 8–18-Micrometer (555–1195 cm^{-1})

The dominant emissions in the 8–18.0-μm passband are O_3 (9.6 μm) and CO_2 (15 μm). However, at altitudes above 100 km, the O_3 emission falls off very rapidly, and thus, the 15-μm CO_2 band becomes the only significant radiator in this passband. Consequently, in the lower thermosphere, this passband can be considered to be a 15-μm CO_2 filter, which measures variations that are due solely to changes in the CO_2 emission. Figure 22 shows typical day, night, and auroral profiles. The profiles in this passband show considerable variability, especially in the 80–120-km-altitude region. Variability due to ozone similar to that observed for the 8–12-μm passband is apparent near 85 km. Above 100 km variations are due to variability in the atomic oxygen and CO_2 densities. The average NER for this filter passband is 1.8×10^{-10} W/cm^2 · sr. Nearly all of the 8–18-μm profiles exhibit radiance peaks or knees in the 80–120 km region. Many profiles exhibit two peaks, one at about 80–90 km and another at approximately 105–110 km, whereas others show only the upper of these two peaks. Often these features appear as only knees in the profiles, whereas in other cases they appear as actual peaks. In either case, these features are observed for both day and nighttime conditions and for all latitudes. The emission above 110 km was found to be enhanced in the daytime and at high latitudes relative to nighttime midlatitudes. At present, there are no known mechanisms for chemical production of CO_2 in excited states that can explain these observations. We do not believe that these enhancements above 110 km can be attributed to atomic oxygen density or temperature effects. Consequently, we suggest that these observed enhancements in CO_2 radiance are most likely the result of variations in CO_2 density resulting from vertical winds induced by Joule heating and wave activity.[34]

In the mesosphere, emission from the 9.6-μm (ν_3) band of O_3 makes a significant contribution to the overall radiance observed in this passband. As a result of this, the 15-μm emission from CO_2 in the mesosphere can only be estimated by subtracting the radiance measured in the 8–12-μm passband for a nearby scene from the value observed for the 8–18-μm band. A more comprehensive and unambiguous set of 15-μm CO_2 data have been collected for the mesosphere and lower thermosphere by the SPIRIT III sensor on the MSX satellite experiment.[14]

Radiometer Filter 6 Data, 17-Micrometer Long Pass (420–565 cm^{-1})

Emissions due to pure rotational transitions of water vapor are the only important emissions in the 17–24-μm passband. Profiles in this passband are characterized by steadily diminishing radiance from the ground to approximately 80 km. There is little diurnal variability observed for this emission, however, a latitudinal variation was observed. These profiles were found to be in good agreement with profiles generated by using the SHARC atmospheric radiance model up to about 80 km where the observed profiles flatten out and the emission becomes dominated by NRER (see earlier discussion on telescope off-axis leakage) and eventually by collisionally excited near-field water contamination.[30] Typical filter six radiometric profiles are shown in Fig. 23. The average NER for this filter passband is 1.2×10^{-10} W/cm^2 · sr.

Summary of the Minor Species Measured by CIRRIS

Trace Gases of the Mesosphere and Lower Thermosphere

In this section we collect and summarize the results reported elsewhere by various authors.

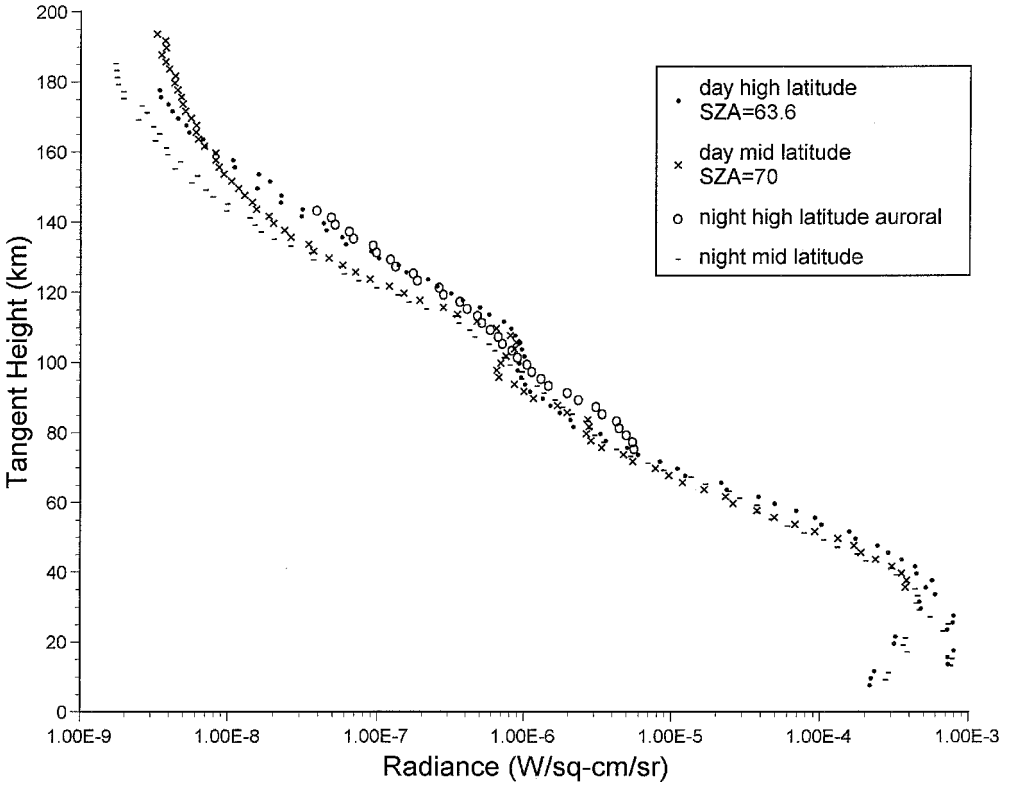

Fig. 22 Radiometric profiles for the 8–17-μm passband.

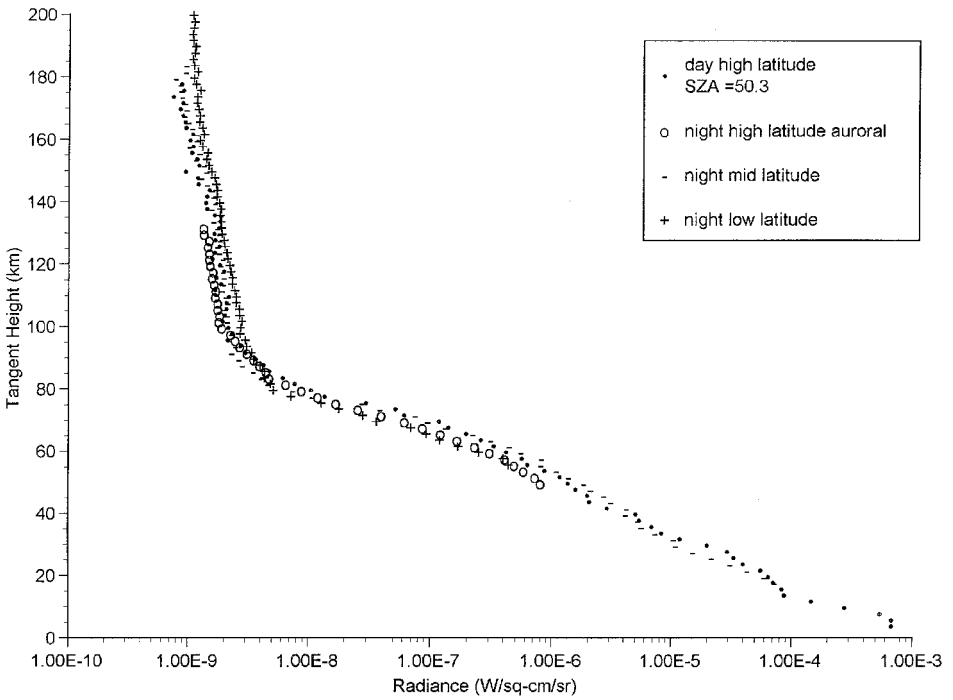

Fig. 23 Radiometric tangent height profiles from the 17-μm long pass filter.

CO. Dodd et al.[24] have analyzed the emission from CO in the 4.7-μm region between 70 and 150 km and have reported absolute column radiances for $^{12}C^{16}O$, $^{13}C^{16}O$, and $^{12}C^{18}O$. The minor isotope column radiances are up to 30 times more intense than predicted, based solely on the natural isotopic abundances of ^{13}C and ^{18}O, with greater relative importance at night. These isotopes are optically thin and efficiently pumped by the warm Earth surface. The Atmospheric Radiance Code (ARC) line-by-line non-LTE code was used to calculate the CO vibrational temperatures and the resulting band limb radiance, based on a spectral fitting technique. Synthetic basis functions were calculated for various rotational temperatures, with positions from the HITRAN92 database[38] fitted to the $^{12}C^{16}O$. The radiance profiles for day/night conditions are shown in Fig. 24 along with model results (Winick, private communication). Daytime CO limb radiances are about seven times brighter than corresponding nighttime cases. The data indicate that current climatology databases underestimated CO above ~70 km. Lower atmospheric boundaries (ground and clouds) can be a predominant excitation source for weak, isotopic bands.

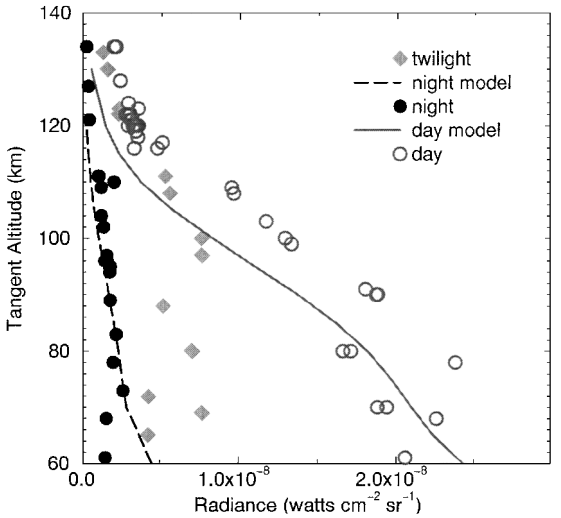

Fig. 24 CO limb emission profiles obtained from interferometer data (courtesy of Jeremy Winick).

CO_2. CO_2 emissions observed at both 4.3 and 15 μm in the lower thermosphere exhibited strong latitudinal dependencies for both night and daytime conditions. This was probably due to the high geomagnetic activity that occurred before and during the CIRRIS observations resulting in increased CO_2 concentrations in the lower thermosphere from vertical winds generated by Joule heating.[34] In the daytime, the high/midlatitude ratio of the 4.3-μm emission varied from about 2.6 at 120 km to about 5.8 at 140 km. Because of the high-inclination orbit of the STS-39 mission, this variation in CO_2 emission was due to the variation in latitude and SZA. The SZA dependence was due to the radiative excitation from the upper mesosphere, which itself exhibits a strong SZA dependence (due to the opacity effects on solar pumping). When the effects of this upwelling emission are incorporated, it was found that the CO_2 density declines by about a factor of 4 between high and low latitudes at 140 km (independent of SZA) and by about a factor of 2 at 120 km (for $K_p \cong 5$) (Winick, private communication). Similar results are evident from analysis of the CO_2 data in the 15-μm region.

H_2O. Emissions from atmospheric water are found throughout most of the IR spectrum for tangent altitudes up to about 85 km. Vibrational emissions from water occur in both the 2.7- and 6.3-μm regions. The ν_2 fundamental band at 6.3 μm was observed with the CIRRIS interferometer (filters 0 and 3) and with the 6–9-μm radiometer filter band (filter 3). Pure rotational water vapor emissions in the 17–22-μm region were also measured with both the interferometer (filters 0 and 6) and radiometer (filter 6). Spectral simulations performed using the SHARC and SAMM atmospheric radiance models were found to be in good agreement with CIRRIS observations.[30,39] Typically, this agreement was better than 30% over the observed tangent height range in both the ν_2 and pure-rotation wavelength regions. In addition to atmospheric water, near-field contamination from collisionally excited water outgassed from the shuttle was also observed at tangent altitudes above ~85 km (details are given in the section on contamination).

NO. Emissions from NO were observed in both the fundamental and overtone band regions. These data have been analyzed and reported by a number of authors.[35,36,40,41] Several important discoveries were made from analysis of the CIRRIS-1A spectra in the fundamental band region around 5.3 μm (Refs. 35, 36, and 40). One of these is the identification of R-branch rovibrational bandheads. The first two bandheads ($v = 1$ and 2), which are located at 2020 and 1990 cm^{-1}, respectively,[35,36] are prominent features in the daytime spectra, particularly at high latitudes and also at nighttime in the auroral zone (see Figs. 9 and 11). Although not as easily apparent in the nighttime spectra for low and midlatitudes, Smith and Ahmadjian[35] have confirmed the presence of bandheads in the spectra for these conditions as well, by analyzing coadded interferograms. The spectra in this region have been interpreted as a superposition of two components: one that is rotationally thermalized and one that is characterized by a nonthermal rotational distribution with very high rotational excitation where $J_{max} \geq 82$. This nonthermal rotational component is excited both vibrationally and rotationally and can be characterized by rotational temperatures in the range of 2500–5000 K. Smith and Ahmadjian[35] identified R-branch bandheads for vibrational states up to $v = 1-10$. These highly rotationally excited emissions in NO have also been observed in the artifically excited atmosphere by an IR interferometer flown on a rocketborne electron beam experiment (EXCEDE III).[42] These authors reported rotational bandheads corresponding to vibrational levels up to $v = 12$ and rotational temperatures in the range of 4500–8000 K. Lipson et al.[40] used nonlinear least-squares spectral fitting to analyze the thermalized component of the NO fundamental band in the CIRRIS spectra and found that the spin-orbit distribution represents a third degree of freedom, along with vibration and rotation, that is not in equilibrium with the local kinetic temperature. This subthermal distribution is most likely produced by the collisional uppumping of NO ($v = 0$) by O atoms, which is the major source of NO ($v = 1$) in the thermosphere. Determination of the kinetic temperature from the rotational envelope of the thermalized component has been examined by Sharma et al.,[43] Dothe et al.,[44] Duff and Sharma,[45] and Sharma and Duff[46] for altitudes above 130 km. Sharma et al.[43] found that the rotational envelopes could be adequately described by Maxwell–Boltzmann distributions. The temperatures derived by these authors were typically 25% lower than those predicted by the MSIS model at most altitudes.[46] Analysis of NO spectra for altitudes below 80 km was complicated by the presence of competing emissions from water (ν_2) and from two O_3 combination bands. Armstrong et al.[36] developed a model from their analysis of the fundamental band, which they used to predict NO emissions for the two components in the overtone band. They concluded that this region would be dominated by the nonthermal component. These predictions have recently been confirmed by Smith.[47]

NO^+. Although NO^+ is the dominant positive ion below 170 km in the thermosphere during the day, its atmospheric emission spectrum in the IR has been somewhat difficult to measure due to the coincidence of its fundamental band (2344 cm^{-1}) with the very strong CO_2 (ν_3) emission band at 2349 cm^{-1}. Nevertheless, NO^+ was tentatively identified in the emission spectra of an overhead aurora obtained by the field-widened interferometer rocketborne experiment[48,49]; however, the observed signal was very close to the noise level of the instrument. This problem was overcome in the CIRRIS experiment due to the superior sensitivity of the CIRRIS-1A interferometer, and unambiguous spectral identification of NO^+ in the atmospheric emission spectra was made for the first time. NO^+ was clearly observed not only for high-latitude auroral conditions, but also for daytime conditions as well. Emissions from NO^+ for low/midlatitude conditions were more difficult to discern from the nighttime spectra but were clearly evident even with weak auroral dosing at high latitudes. The presence of NO^+ emissions for low/midlatitude nighttime conditions was confirmed by analysis of coadded spectra. In general, quiescent nighttime NO^+ emissions are about an order of magnitude weaker than daytime emissions, and emissions at low latitude are weaker than emissions at high latitudes.

Analysis of CIRRIS-1A data has indicated that NO^+ is the dominant radiator in the 4.3-μm regions for tangent altitudes above about 140 km in the daytime.[50,51] The authors of Refs. 50 and 51 reported that the vibrational distribution ($v \leq 2$) was consistent with NO^+ production dominated by the $N_2^+ + O \rightarrow NO^+(v) + N(^2D)$ reaction in agreement with the conclusions reported by Caledonia et al.[52] from recent rocketborne auroral radiometric measurements. More recently, Smith et al.[53] have reported that a significant fraction of the NO^+ emission is from highly rotationally excited NO^+ (v, J), where $J \geq$ approximately 90. This non-LTE rotationally excited component was observed for both quiescent and aurorally disturbed conditions.

O_3. Ozone emissions in the ν_1 and ν_3 fundamental bands at 9.1 and 9.6 μm, respectively, were observed with several interferometer filters (0, 3, and 7) and radiometer filter 7 (8–12 μm). These data have been analyzed to retrieve O_3 density or VMR profiles in both the stratospheric[22] and mesospheric[54] regions. Generally,

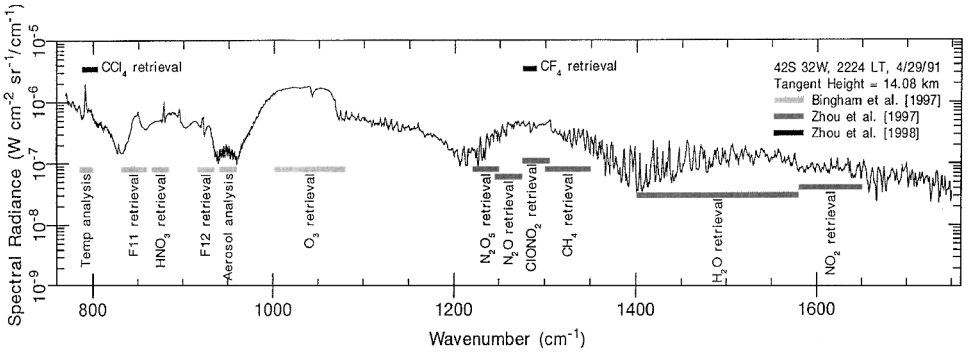

Fig. 25 Example of stratospheric IR emission spectrum collected at 2224 LT 29 April 1991, at a tangent height of 14.1 km, latitude of 42°S, longitude of 32°W, by CIRRIS-1A interferometer detector 5, filter 3.

these profiles were found to be in good agreement with previously reported measurements by others.[55–57] Zhou et al.[54] inverted CIRRIS limb radiance profiles to retrieve the (001) excited state populations that were in turn used, in conjunction with the modeled vibrational temperature, to estimate the total ozone density profiles. The mesospheric profiles derived from the CIRRIS observations showed a strong diurnal variation and a clear secondary maximum near 88 km. However, the derived ozone concentration was roughly two times larger than that predicted by the recent two-demensional photochemical model of Garcia and Solomon.[58] Zhou et al.,[54] also estimated the daytime ozone photodissociation rate. Lowell et al.[59] used the (001)–(000) band to retrieve the kinetic temperature profile in the 70–110 km region, assuming the closely spaced rotational levels to be strongly collisionally coupled, given mean collision time (10^{-4} s at 90 km) and radiative lifetime of 10^{-1} s.

Spectra of ozone hot band chemiluminescence in the υ_3 band were also obtained with the CIRRIS interferometer (filters 0, 3, 5, and 7) and radiometer (filter 5). These NLTE emissions from highly vibrationally excited ozone are an important source of radiation in the 10–12.5-μm region in the mesosphere. The high-lying vibrational levels responsible for these emissions are populated in ozone production resulting from three-body recombination of O and O_2. The spectra observed in this region show considerable spectral structure; however, most, if not all, of this structure can be ascribed to pure rotational transitions from highly rotationally excited OH. These OH emissions are described in more detail in the next section. A state-by-state intrepretation of the CIRRIS O_3 (υ) spectra has not been performed, but is clearly complicated by the presence of these OH features. However, the absence of spectral structure in this region that can be associated with O_3 hot bands appears to indicate a high degree of vibrational mode mixing or hot rotational distributions as suggested previously by Rawlins et al.[57]

OH. IR emissions from OH were observed in all of the interferometer filter passbands (filters 0, 1, 2, 3, 5, 6, and 7). As a result, a large number of OH Earthlimb spectra were collected in several spectral regions. Fundamental band vibration/rotation emissions from OH ($\upsilon = 1-9$) and pure rotational emissions from highly rotationally excited OH ($N = 13-33$) were observed between tangent heights of 80 and 110 km for both daytime and nighttime quiescent conditions.[25] These data were analyzed in the 430–575 cm^{-1}, 780–1000 cm^{-1}, and the 2100–3750 cm^{-1} spectral regions by Dodd et al.[26] to derive OH (υ, N) absolute population column densities and the relative populations for the four spin sublevels. This analysis indicated equal populations in the two spin-rotation states, but a preferential population of the $\Pi(A')$ Λ-doublet state leading to a $\Pi(A')/\Pi(A'')$ ratio of 1.8. Smith et al.[25] gave several possible sources for the highly rotationally excited OH (υ, N). These were 1) direct chemical production by the $H + O_3$ reaction, 2) collision-induced transfer of vibrational to rotation energy, that is, V/R transfer, from nascent OH high-υ states, and 3) excitation of thermal OH ($\upsilon = 0$) by translationally excited (fast) oxygen atoms (O_f). Dodd et al.[60] examined these and other possible sources and concluded that mechanisms 1 and 2 were both consistent with all aspects of the CIRRIS OH (υ, N) observations, but that other possible sources could be eliminated from consideration. In addition, these authors suggested the possibility that the two separate channels suggested by Kaye[61] for the $H + O_3$ reaction might preferentially populate high-υ and high-N levels of OH, respectively. Further study will obviously be required to identify which of these two possible sources is the correct mechanism.

In addition to the spectral data discussed, OH emissions also contributed to the in-band radiance observed in six of the eight radiometer filter passbands (FP1, filters 0, 1, 5, 6, and 7 and FP2). At night, OH emissions dominated the radiance in the FP2 filter passband (2.5–3.4 μm). As a result, a large number of OH radiance vs tangent height profiles were obtained during the CIRRIS mission. These profiles were discussed in an earlier section.

Trace Gases of the Stratosphere

In this section we summarize the results reported previously by several authors.[22,54,62–64] More than a dozen important stratospheric species (greenhouse gases) were measured simultaneously by the CIRRIS interferometer. These species include CO_2, CFC-11, HNO_3, CFC-12, O_3, N_2O, NO_2, N_2O_5, CH_4, $ClONO_2$, H_2O, CF_4, and CCl_4, all of which emit in the 5.5–13 μm region. A typical CIRRIS stratospheric spectrum in this spectral region is shown in Fig. 25.

Unfortunately, only a small portion of the mission was allocated to the collection of vertical Earthlimb radiance profiles in the atmospheric window regions using a step-stare (vertical staircase) data collection mode. In addition, remember that the CIRRIS-1A experiment did not carry ancillary sensors designed to provide the temperature, pressure, and aerosol measurements necessary to retrieve the trace gas volume mixing ratios directly from the IR data. As a result, the analysis and retrievals were performed by using the National Meteorological Center temperature–pressure profile closest to the measurement in time and space. Details of the specal analysis, the density profile retrievals, and the error analysis are found elsewhere.[34,62,64] VMR profiles were retrieved from the CIRRIS spectra utilizing an onion-peel retrieval method that used FASCOD3[65] with HITRAN92 database[38] to provide the synthetic comparison spectrum. The horizontal bars in Fig. 25 indicate retrieval regions used by Bingham et al.[22] and Zhou et al.[62,63] to obtain the VMR profiles for the various species.

Recently, an optimal numerical temperature and constituent retrieval code was developed and applied to the CIRRIS-1A data.[64] This code utilized an efficient derivative of FASCODE 3, in conjunction with the HITRAN96 database,[66] coupled to an optimal estimation inversion method. This code allowed for the simultaneous retrieval of middle atmospheric temperature and trace gas species VMR profiles with significantly reduced errors. In addition to the trace species mentioned earlier, this code found clear evidence for the presence of several additional species in the CIRRIS-1A spectra. These species include SF_6, HNO_4, and several additional CFCs such as $CHCl_2F$ (F21), $C_2Cl_2F_3$ (F113), and $C_2Cl_4F_4$ (F114). Unfortunately, the signatures of these species were either very weak or were apparent at only the lowest tangent heights available in the CIRRIS database (15 km or less). As a result, accurate stratospheric profiles for these species could not be retrieved. Initial daytime temperature retrievals using the CO_2 laser bands (940–960 cm^{-1}) produced exaggerated temperatures above 50-km altitude due to significant

non-LTE contributions from the upper stratosphere. These non-LTE effects were later accounted for by Miller et al.,[67] who used a non-LTE compensation technique to retrieve accurate daytime temperature profiles from the CIRRIS data in the CO_2 laser band region.

Significant diurnal variations were observed for several species (N_2O_5, NO_2, and $ClONO_2$) in agreement with previous observations by others. The VMR profiles for a number of stratospheric species also exhibited differences that are believed to be due to hemispheric variations. However, it must be remembered that (due to orbital limitations) nearly all data collected for the northern hemisphere were for daytime conditions, whereas the southern hemispheric data corresponded to nighttime conditions. As a result, all differences in the VMR profiles must be considered as due to a combination of both latitudinal and diurnal effects.

The CIRRIS stratospheric measurements are important because they occurred only a few weeks before the eruption of Mount Pinatubo (June 1991), which drastically changed the stratosphere for a number of years thereafter. Consequently, these measurements serve as a baseline against which various post-Pinatubo observations can be compared.[68–70] In this way, the short- and long-term effects of a major volcanic eruption on the stratosphere can be accurately assessed. In addition, these data fill an important gap in the measurements between the LIMS (1979)[71–73] and ATMOS (1985)[74,75] and the more recent ATMOS (1992),[69] UARS,[68,76] and EASOE[70,77] data sets.

VMR profiles for various stratospheric species retrieved from CIRRIS spectra were in excellent agreement with previously reported results from other investigators.[78–84] The major findings and conclusions from these investigations are summarized as follows.

1) The use of the CO_2 laser band at 940 cm^{-1} provided an effective way to estimate aerosol emissions in the retrieval of greenhouse gas profiles.

2) Aerosol densities in the pre-Mt. Pinatubo eruption period were found to be very low, as expected for a period with low volcanic activity.

3) The average annual global increase of CFC-11 and CFC-12 in the stratosphere was found to be continuing at a rate of about 5% per year.

4) The average annual global increase of CF_4 and CCl_4 near the tropopause was estimated at approximately 2 and 3% per year, respectively.

5) Linear relationships between several of the long-lived trace gases (CH_4, N_2O, and CFC-12) were observed as predicted by the two-dimensional model calculations of Plumb and Ko.[85]

The successful retrieval of the VMR profiles for a number of very weakly emitting, minor trace gases such as N_2O_5, $ClON_2$, CF_4, and CCl_4 from the CIRRIS database has demonstrated the extremely high quality of this data set and the usefulness and accuracy of the FASCOD3/HITRAN model and database. It is clear from the success of this effort that a set of broadband, high-precision spectral measurements with moderate resolution, when used in conjunction with a high-accuracy model, can provide adequate data for the long-term monitoring of a large number of important greenhouse gases.

Auroral Emissions

The CIRRIS auroral data collections occurred during periods of moderate to active (4- $< K_p <$ 7-) geomagnetic activity (see Fig. 2). Aurorally produced emissions were observed for NO (at 2.7 and 5.3 μm) and CO_2 and NO^+ (both at 4.3 μm). Enhancements were also observed in CO_2 emission in the 15-μm region, but these are believed to be due to Joule-heating-induced vertical lift of CO_2 rather than any direct excitation mechanism.[34] Spectral enhancements of the NO bandheads have previously been discussed by Smith and Ahmadjian[35] and Armstrong et al.[36]

The brightest auroral emissions were observed in 4.3-μm CO_2 and in 5.3-μm NO bands. The high-latitude nighttime radiance profile in Fig. 18 for aurorally disturbed conditions shows the dramatic enhancement effect of particle precipitation on CO_2 and NO^+ in the 4.3-μm region. In the lower thermosphere above 100 km, the auroral enhancements in this spectral region are due mainly to enhanced production of NO^+ because the transfer of vibrational energy from N_2 to CO_2 can take an hour or greater at these altitudes. Below 100 km, the N_2 vibrational transfer to CO_2 is more efficient, and there is also much less NO^+. Large enhancements in the radiance in the NO ($v = 1$) fundamental band were also observed for aurorally active conditions (see Fig. 19). In many cases the high-latitude auroral radiances exceeded those observed for high-latitude daytime conditions.

In the lower thermosphere at altitudes above 100 km, NO overtone emissions at 2.7 μm were observed during high-latitude aurora, making this channel an effective auroral diagnostic tool. The 3914Å and 5577Å emission channels were also elevated during these periods, thus confirming the presence of auroral excitation.

The possibility of direct auroral excitation of O_3 has been suggested by Rawlins et al.[57,86] from analysis of spectra in the 9.6-μm region from two separate rocketborne auroral measurements. Enhancement of O_3 ($v \geq 3$) number densities in the vicinity of a strong auroral arc was suggested as one possible explanation for a discrepancy between full-limb and partial-limb column density results observed in the SPIRIT 1 experiment.[86] These conclusions are consistent with observations of electron beam-enhanced O_3 (ν_3) emission reported by Paulsen et al.[42] during an artificially induced aurora. Unfortunately, a detailed analysis of the CIRRIS auroral spectra in the ozone hot band region has yet to be carried out. As a result, these potential auroral effects on ozone emissions have not been confirmed by CIRRIS observations and, thus, for the time being remain inconclusive.

Terminator Crossing Data

The CIRRIS-1A sensors collected data during both sunrise and sunset terminator crossings. However, the data collected from the sunset terminator crossings were more useful because the LOS was oriented parallel to the terminator during these crossings. Preliminary results from these terminator data collections were first reported by Smith et al.[87] In most cases, the structure observed near the terminator was due to diurnal variations. Abrupt changes (of a factor of 2–4) were observed near the mesopause in the 2.7-μm (OH) and 8–12-μm (O_3) filter bands. The OH band exhibits a sharp increase of about a factor of 4 at the dusk terminator, whereas the O_3 band shows a similar abrupt increase of around a factor of 2.5. The 8–12-μm band radiance is lower during the daytime due to ozone photolysis, but this is partially offset by contributions from O_3 hot bands and solar excited CO_2 laser bands. OH production is primarily from the $H + O_3$ reaction and, thus, decreases rapidly after dawn due to depletion of O_3. A slow increase of about a factor of 3 in OH radiance during the day is attributed to an increase in ozone due to O atom photoproduction and to an increase in H atoms.[39] The observed variations across the terminator in the 2.7-μm band have been closely simulated using the OH model of Makhlouf et al.[33] In the mesosphere, large diurnal variations ($\sim \times 100$) were also observed in the 4.3-μm CO_2 band. It is well known that NO also exhibits a large diurnal variation, but this variation was not discernible close to the terminator in the CIRRIS data. This is probably because changes in the 5.3-μm emission are mainly due to increases in NO density rather than a solar fluorescence mechanism (such as is the case with 4.3-μm CO_2). However, significant spatial structure was observed in the 5.3-μm band near the edge of the auroral oval. Several bands, including the 6–9-, 11–13-, and 17-μm long pass window bands, showed almost no variation near the terminator.

Downward-Viewing Backgrounds

Below the Horizon Spectra

Downward-looking observations of the Earth background were obtained over the United States from Baja California, Mexico, to Ontario, Canada. Spectral data were collected for both cloudy and clear conditions, primarily in the 4.9-μm short-pass optical filter. Figure 26 compares spectra obtained in the mid-wave infrared (MWIR) region for two different cloud cover conditions. The emission in the heart of the band is optically thick and, thus, originates from the same altitude in both spectra. Spectral data of this type can be useful for space surveillance applications in the MWIR. Blackbody radiation from the warm Earth surface dominates the spectrum for broken cloud conditions, whereas when denser clouds are present, these clouds attenuate the emission from the Earth's surface

and thermal emission from the cooler clouds is the dominant source. On the short wavelength side of the band, the emission is due to a combination of thermal emission and solar scattering components. The atmosphere is opaque in the heart of the CO_2 band near 4.3 μm and, therefore, the sensor is unable to view the ground. The emission in this region originates from an altitude of about 20 km and thus is invariant for the different cloud conditions. A typical CIRRIS below-the-horizon (BTH) spectrum in the 4.3-μm region was modeled by Adler-Golden et al.[39] using both LTE (MODTRAN) and non-LTE (SAMM) atmospheric codes. Significantly better agreement was obtained using the SAMM model, thus indicating the importance of non-LTE effects in modeling upwelling radiation in the 4.3-μm region of the IR. A typical example of a downward-looking background spectrum obtained with the open filter (filter 0) is shown in Fig. 27.

Spatial Structure in BTH Backgrounds

Spatial structure in the nadir-looking backgrounds from CIRRIS has been well characterized by several groups.[88–95] The goal of these studies was to characterize background clutter against which surveillance systems must detect missile and plume signatures. An example of the spatial structure observed in the 2.7- and 4.3-μm bands (collected simultaneously) is shown in Fig. 28. The 2.7- and 4.3-μm bands are either correlated or anticorrelated, depending on the presence of clouds and the SZA. Note the transition from terrain to cloud background, which occurs at appoximately 60 s. When clouds are present, the 2.7-μm band (2.5–3.4 μm) is dominated by scattered sunlight off of the clouds, whereas the 4.3-μm band (4.2–4.6 μm) is dominated by thermal emission from the cloudtops. Because these clouds are cooler than the Earth's surface, the emitted radiance in the 4.3-μm band is lower than when clouds are absent. This generally results in anticorrelation between the 2.7- and 4.3-μm channels. We use the term anticorrelation here to mean a high degree of negative correlation as opposed to no correlation. When no clouds were present, the emittance from the Earth's surface could be detected in both bands, and the emission in these two bands was generally correlated. However, atmospheric absorption along the LOS must also be considered, particularly in the case of the 4.3-μm band.

CIRRIS Celestial Observations

Three stars were observed by the CIRRIS-1A radiometer. These were α-Scorpio (Antares), α-Bootes, and α-Centauri. The in-band radiances measured for these stars are summarized in Table 5. Measurements of α-Scorpio were obtained in all of the radiometric filter passbands. The in-band radiance of α-Scorpio in the 8–17-μm band was within 10% of a similar measurement made by the IRAS experiment.[96]

In addition, α-Bootes was also measured in a number of different radiometric passbands. The 6–9 μm measurement can be compared to the in-band irradiance specified for the MSX/SPIRIT III Band A (6.8–10.9 μm) of 1.45×10^{-14} W/cm^2 (Ref. 97). The CIRRIS radiometer detector FOV is approximately 1.5×10^{-6} sr, which gives an in-band irradiance of 1.8×10^{-14} W/cm^2.

A chance observation of α-Centauri by the IR radiometer occurred close to the sunrise terminator during an auroral measurement mode (PC42B) near the end of orbit 20. The point source emission in the 6–9-μm band could be discerned above the rising background emission. These results are also shown in Table 5.

CIRRIS Measurements of Shuttle-Induced Contamination

Before the STS-39 shuttle mission, there was still much debate over the acceptability of the space shuttle as a platform for conducting sensitive IR measurements. This debate was fueled in part by mass spectrometer measurements from an earlier mission (STS-4), which recorded significant levels of gaseous water contamination in

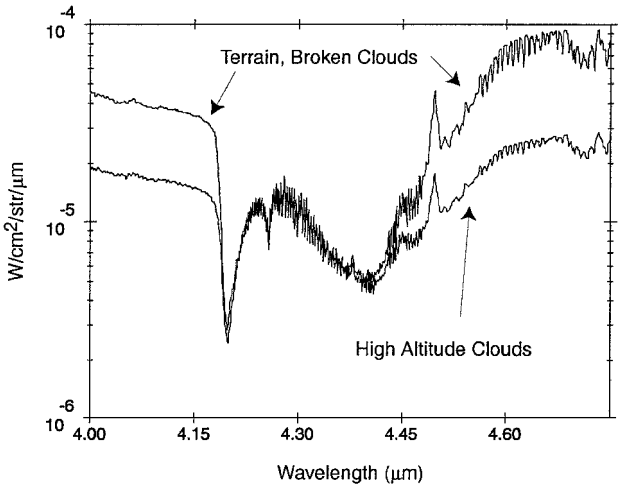

Fig. 26 Examples of downward-looking spectral data from the CIRRIS interferometer in the MWIR (4.3-μm) region.

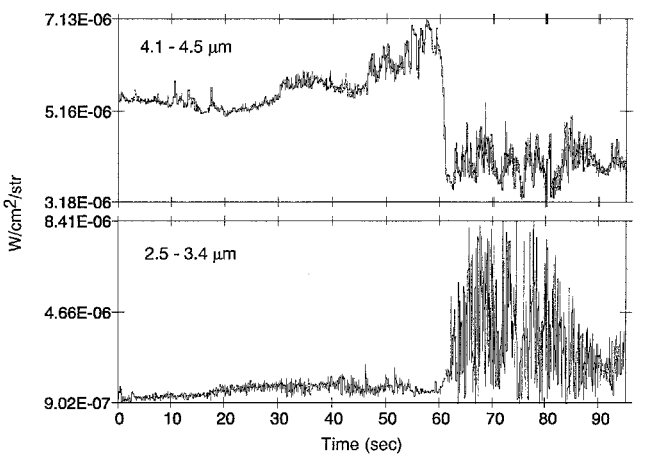

Fig. 28 Cloud and terrain structure in downward-looking radiometric data in the 2.7- and 4.3-μm regions.

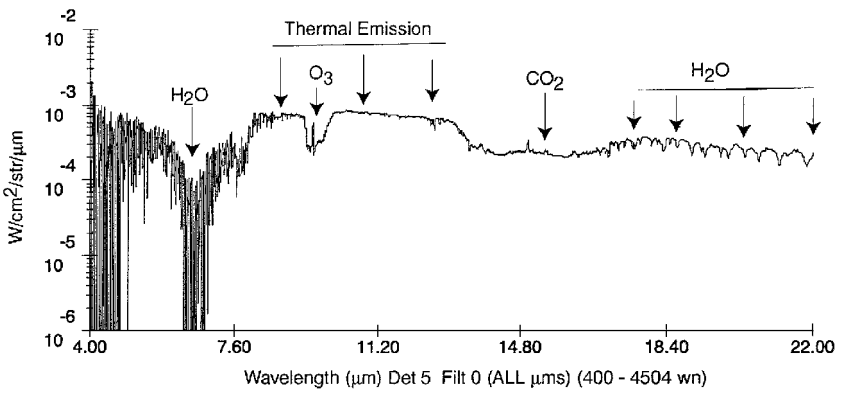

Fig. 27 Typical interferometer spectrum of a downward-looking background obtained using the open filter (Filter 0); note the absorption features due to water, ozone, and carbon dioxide near 6.3, 9.6, and 15.0 μm, respectively.

Table 5 In-band radiances (W/cm^2· sr) measured by the CIRRIS-1A radiometer for the stars α-Bootes, α-Centauri, and α-Scorpio

	Radiometer filter passband, μm							
Star	2.5–3.4	4.1–4.5	4.9–7.1	6–9	8–12	11–13	8–17	17 LP
α-Scorpio	2.0E−07	3.0E−08	5.0E−08	3.3E−08	2.0E-08	5.5E−09	2.0E−08	2.7E−09
α-Bootes	7.2E−08	1.36E−08	2.0E−08	1.2E−08	—	—	6.6E−09	—
α-Centauri	1.0E−07	—	—	1.05E−07	—	—	—	—

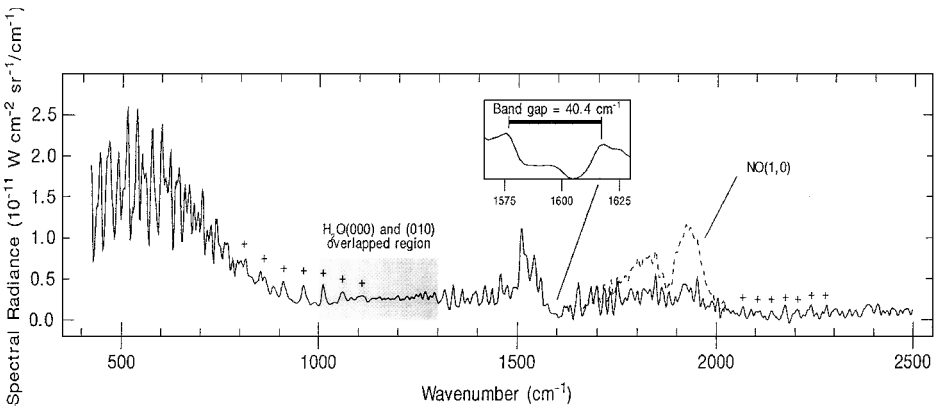

Fig. 29 IR shuttle glow spectrum in the 450–2500 cm^{-1} region.

the near-field shuttle environment.[98,99] Considerable attention was also paid to the subject of shuttle glow, as a result of the initial report by Banks et al.[100]

In addition, the interaction between contaminants outgassed from the shuttle and other low-Earth-orbit (LEO) platforms and the ambient atmosphere was expected to produce background emissions of sufficient magnitude to impact the sensitivity threshold for measurements taken with IR sensors mounted on these platforms.[101–105] In particular, translation/vibration (T/V) and translation/rotation (T/R) energy transfer resulting from energetic collisions between IR-active shuttle effluents and ambient atoms or molecules in the atmosphere was expected to be an important source of shuttle-induced IR emission under LEO flight conditions.[103,105] The first IR observations of shuttle-induced contaminants were reported by Koch et al.[106] from measurements made by a helium-cooled infrared telescope (IRT) flown on STS-51F (Spacelab 2, 1985). However, before the CIRRIS observations on STS-39, relatively little was known about the IR environment of the space shuttle.

IR spectral measurements obtained by the CIRRIS-1A interferometer for high tangent altitudes and positive elevation angles (Fig. 29) showed clear evidence of emissions in the 4–25 μm region, which were not attributable to atmospheric sources.[16,30,31] [In Fig. 29, the characteristic H_2O (010) band gap is illustrated in the inset. The shaded interval identifies the primary region of overlap for the ν_2 fundamental and pure-rotational emissions, and the dashed curve (1650–2000 cm^{-1}) illustrates the NO (1, 0) contribution to the uncorrected data. Positions of H_2O high-J transitions are indicated with pluses.] The CIRRIS-1A cryogenically cooled telescope was designed to achieve very high off-axis rejection, and this design proved to be quite effective in minimizing the contribution of out-of-field-of-view radiation (leakage) from the lower atmosphere and the hard Earth relative to the very weak signals measured in the high-altitude Earthlimb scans. Based on an analysis of Earthlimb and bay-to-space data, Dean et al.[30] concluded that the residual signals observed in the very high Earthlimb were not due to inadequate off-axis rejection of the telescope system, but were instead produced in the near field of the shuttle by outgassed water vapor (mostly from the shuttle tiles) that had been vibrationally and rotationally excited by collisions with ambient atmospheric atomic oxygen. Considerable translational energy (about 3 eV) is available from these collisions for energy transfer to excite the IR-active water molecules. This excitation results in average effective temperatures that are very high (2000–2200 K) (Refs. 30 and 32). The effect of these high temperatures is to produce a spectrally extended H_2O emission spectrum that extends continuously throughout the entire IR spectral region from 2 to 40 μm. In addition, numerous spectral peaks corresponding to known positions of high-J transitions in the pure rotational and ν_2 regions were identified in these spectra.[107,108]

Zhou et al.[109] developed an IR contaminant model to investigate the shuttle-induced excitation and emission of water molecules outgassed from the space shuttle. This model was utilized by these authors to simulate the near-field measurement environment for the STS-39 (CIRRIS-1A) and STS-51F (IRT) shuttle missions for both normal outgassing and water dump conditions. This study estimated that approximately 1.4×10^{27} H_2O molecules (or 41.5 kg of water) were outgassed from the shuttle before the completion of the CIRRIS measurements at approximately 60 h. mission elapsed time (MET). Starting at an outgassing rate of $\sim 10^{23}$ mol/s (0-h MET) the water contamination decayed rapidly during the first two days (25 h) with a time constant of ~2.5 h, and then decayed more slowly thereafter (with a time constant of ~38 h). However, the CIRRIS instrument cover was not open during the first 20 h of the STS-39 mission. By the time the CIRRIS measurements were begun, the water outgassing rate had dropped to 2×10^{20} mol/s. Unfortunately, these results can not be considered as typical of other space shuttle missions because the amount of water carried into space by the shuttle tiles is highly dependent on prelaunch weather conditions, which can vary significantly from one flight to another. The CIRRIS measurements showed enhanced brightness from behind the orbiter. This observation is consistent with the model calculations of Zhou et al.,[109] which indicate that most of the H_2O molecules are excited in front of the shuttle and are then stripped back away from the source to the downstream region. During normal outgassing periods (with water outgassing rates $< 5 \times 10^{22}$ mol/s), these authors also concluded that most of the H_2O molecules were excited by collisions with ambient oxygen. On the other hand, during high outgassing periods (such as water dumps) the large amount of water released shields the oxygen atoms from the source of the H_2O molecules and, therefore, many water molecules in the center of the cloud do not collide with ambient oxygen atoms and are, thus, not excited.

In addition to the gaseous contamination discussed earlier, particulate contamination effects were also occasionally observed during the CIRRIS mission. The particulate environment surrounding the shuttle during the CIRRIS mission was studied by Green et al.[110] using data from both the interferometer and radiometer. Although these authors concluded that the STS-39 environment was generally

quite benign, several discrete particle events were nonetheless observed. Using particle radiances, spectral distributions, and blur circle sizes, these authors estimated particle sizes and ranges. Despite an estimated particle size detection threshold of ~50 μm, the particles observed were all in the range of a few hundred micrometers to several centimeters.

Nonthermal Emissions from Highly Rotationally Excited Species

Prior to the CIRRIS experiment, atmospheric radiance models and codes assumed that atmospheric species were in rotational equilibrium at the local kinetic temperature (LTE). The excess energy from exothermic reactions was assumed to go primarily into translation and vibrational excitation of the reaction products. In fact, this LTE assumption is the basis for various techniques that utilize the rotational distribution (envelope) to derive local atmospheric temperatures. The CIRRIS data have clearly demonstrated that this assumption is not always valid in the mesosphere and the thermosphere and, furthermore, that it is generally not the case for diatomic species.

Among the most significant scientific discoveries to come from the CIRRIS experiment was the identification of important new non-LTE emissions from several highly rotationally excited diatomic species in the mesosphere and thermosphere. These nonthermal (high-J) rotational emissions were observed for OH, NO, and NO^+ for both day and nighttime conditions. The presence of these non-LTE rotational emissions greatly increases the spectral extent of the IR signatures from these important atmospheric emitters. Whereas non-LTE vibrational excitation extends the emission feature only on the red (long-wavelength side) side of the thermal band, non-LTE rotational excitation extends the emission on both sides of the thermal band. In most cases, these high rotational emissions extend into regions that were previously thought to be atmospheric IR window regions, where they then become the dominant radiators. Taken together these emissions extend nearly continuously throughout the IR from 2.5 to 25 μm. A summary of the spectral extent of these non-LTE rotational emissions is given in Fig. 30.

Rotational bandhead emissions were observed for the fundamental and overtone bands of NO and for the NO^+ fundamental band. Bandheads in the pure rotational spectrum of OH are predicted at 1094 cm^{-1} ($v = 0$, $N = 47$) and 1034 cm^{-1} ($v = 1$, $N = 46$), respectively, by the model of Goldman et al.,[111] but were not observed in the CIRRIS spectra. Non-LTE (high-J) populations in thermospheric CO ($v = 1$) have been predicted by Kutepov et al.[112] at altitudes above 100 km. Indeed, CO ($v = 1$) rotational temperatures derived from CIRRIS data have given temperatures significantly greater (by an average of 300–400 K) than the local kinetic temperatures in the 120–200 km altitude range.[36,44] Consequently, a search for CO bandheads in the fundamental band region of the CO emission spectrum was conducted, but no bandheads were found. However, note that these bandhead emissions are predicted to occur starting at 2326 cm^{-1} ($v = 1$), which is in the region dominated by the very strong CO_2 (ν_3) band at 2349 cm^{-1}.

The high-J/N rotational emissions observed by CIRRIS correspond to very high levels of rotational excitation with minimum rotational energies in the range of 1.4–2.3 eV. Table 6 summarizes the maximum rotational and vibrational levels observed and the corresponding minimum rotational and total internal energies. Typically, these rotational energies exceed the vibrational energies for $v \leq 4$. The fraction of the total internal energy that is in rotational excitation for several selected vibrational levels is given in Table 7.

A summary of the rotational non-LTE emissions observed by the CIRRIS sensors is presented in Table 8. Table 8 lists the species, vibrational and rotational states, and the range of tangent altitudes for which these emissions were observed.

Since the first published reports of these highly rotationally excited emissions in the upper atmosphere, there have been numerous studies undertaken to identify the sources of these non-LTE emissions and to model the emissions. For OH, these studies include those by Dodd et al.,[26,60] Holtzclaw et al.,[113] and Adler-Golden.[114] For NO, these include studies by Sharma et al.,[37,43,115,116] Duff

Table 6 Summary of the bands, vibrational and rotational levels, minimum rotational energy, and total internal energy for non-LTE rotational emissions observed by CIRRIS

Species	Band, Δv	Maximum J or N level observed	Maximum v level observed	Minimum rotational energy, eV	Minimum total internal energy (R + V), eV
NO	1	≥82	9	1.4	3.1
NO	2	≥82	12	1.4	3.7
NO^+	1	≥90	4	1.9	3.0
OH	0	33	6	2.3	3.3

Table 7 Fraction of the total internal energy that is in rotational excitation for various highly rotationally excited species

	Fraction of internal energy in rotation				
Species	$v = 0$	$v = 1$	$v = 3$	$v = 4$	$v = 9$
OH	1.0	0.828	0.613	0.296[a]	——
NO	——	0.803	0.626	0.558	0.33
NO^+	——	0.826	0.641	0.567	——

[a]Maximum N values for vibrational levels above $v = 3$ are typically in the range ~19–31 and fall in the 575–780 cm^{-1} region, which is obscured by the very strong 15-μm CO_2 (ν_2) emission band. As a result, the maximum N values observed are probably not the maximum levels populated. Therefore, the rotational fraction given should be considered as a lower limit for OH ($v = 4$).

Table 8 Summary of the vibrational and rotational levels and tangent height range for which rotational non-LTE emissions were observed by CIRRIS

Species	Band, Δv	v levels observed	J or N levels observed	Tangent altitudes for which high-J emissions were observed, km
NO (v, J)	1	1–10	To at least 82	100–260
NO (v, J)	2	2–12	To at least 82	90–130
NO^+ (v, J)	1	1–4	To at least 90	100–215
OH (v, N)	0	1–6	13–33	78–110

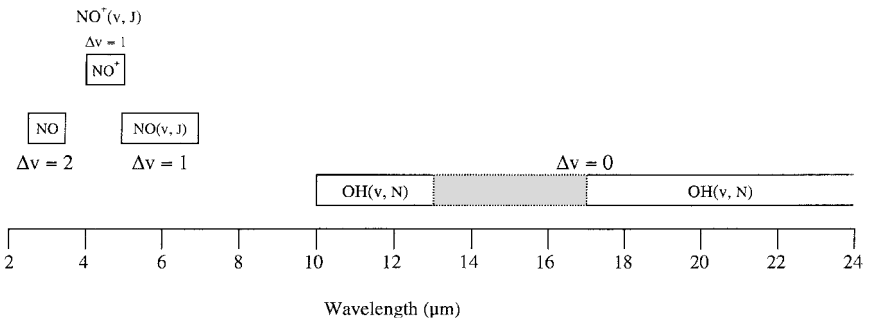

Fig. 30 Spectral extent of non-LTE emissions from highly rotationally excited species observed by CIRRIS.

et al.,[117] Armstrong et al.,[36] Hubert et al.,[118] Duff and Sharma,[119–121] and Dothe et al.[122] A potential source of the highly rotationally excited component of NO^+ was recently investigated by Duff and Smith.[123]

Summary of Major CIRRIS Findings

The CIRRIS experiment was the first global survey of IR emissions in the mesosphere and lower thermosphere. This mission provides a unique set of data that has allowed for significant upgrades of our atmospheric models and has provided guidance for a large number of future space experiments, ground-based investigations, and bandpass selections for space defense systems. The CIRRIS experiment was flown during a solar maximum period in April of 1991, at the peak of solar (sunspot) cycle 22. As a result of this timing, the CIRRIS database serves as an important benchmark against which other measurements can be compared to determine solar cycle variations of numerous species in the mesosphere and lower thermosphere. The coincidental timing of the CIRRIS mission with a major geomagnetic storm was an additional unanticipated benefit that substantially increased the chances of obtaining measurements of highly disturbed auroral backgrounds and resulted in a substantial amount of auroral data being collected. In another bit of fortunate timing, the CIRRIS measurements occurred only a few weeks before the eruption of Mount Pinatubo (June 1991). This was a significant eruption, which drastically changed the stratosphere for a number of years thereafter. Consequently, the CIRRIS stratospheric measurements serve as a baseline against which various post-Pinatubo observations can be compared. In this way, the short- and long-term effects of a major volcanic eruption on the stratosphere can be accurately assessed. The simultaneous data collection by the two radiometer channels and the interferometer resulted in a combination of high spectral and spatial resolution that makes these data unique and has led to important new insights into the chemistry of the upper atmosphere. In addition, these data provided the sources of variability within broad radiometer passbands. We summarize some of the many significant findings to come from the CIRRIS experiment as follows.

There were a number of unexpected and important scientific discoveries that resulted from analysis of the CIRRIS high-resolution Earthlimb emission spectra. Undoubtedly, the most significant of these discoveries was the identification of important new non-LTE emissions from several highly rotationally excited diatomic species (OH, NO, and NO^+) in the mesosphere and thermosphere. These nonthermal rotational emissions were observed for both day and nighttime conditions and were not included in or predicted by existing atmospheric models before the CIRRIS flight. Subsequent studies[60,115,117,123] have shown that several exothermic reactions can produce significant rotational excitation of the reaction products. This seems to be especially true for reactive collisions between energetic (fast) atoms and ions and ambient molecular species. The presence of these non-LTE rotational emissions greatly increases the spectral extent of the IR signatures from these important atmospheric emitters on both sides of the thermal emission band causing them to extend into several atmospheric window regions. Taken together these non-LTE emissions extend throughout a significant portion of the IR region from 2.5 to 25 μm. These emissions are discussed in more detail in the preceding section.

Other findings, discoveries, and conclusions derived from analysis of the CIRRIS data are listed next (not necessarily in order of their importance).

1) There were unambiguous observations of IR emissions from NO^+ in aurora and for the first time in the dayglow and nightglow spectra.

2) Enhanced 15-μm CO_2 emissions were observed at high latitudes, due to enhancements in CO_2 resulting from vertical winds induced by Joule heating.

3) There was discovery of a new IR shuttle glow resulting from collisionally excited outgassed water vapor, which forms an extensive hot contamination cloud surrounding the space shuttle.

4) Nonthermal (subthermal) spin-orbit population distributions were observed for NO ($X^2\Pi$, $v = 1$, $\Omega = \frac{1}{2}, \frac{3}{2}$) in the thermosphere.

5) Preferential population of the $\Pi(A')$ Λ-doublet state was observed for OH from analysis of the pure rotation emission spectra.

6) Many minor stratospheric greenhouse gases were observed, and their concentrations retrieved, thus characterizing the pre-Mt. Pinatubo stratospheric environment. Profiles successfully retrieved include the weakly emitting trace gases N_2O_5, $ClONO_2$, CCl_4, and CF_4, as well as the chloroflorocarbons CFC-11 and CFC-12.

7) Radiances from the two most abundant isotopes of CO ($C^{13}O^{16}$ and $C^{12}O^{18}$) were observed and found to be up to 30 times more intense than predicted, based on their naturally occurring atmospheric abundance.

8) Aurorally enhanced NO emissions are significant in the fundamental and overtone bands and in the 6–9-μm region due to P-branch contributions from rotationally hot NO (v, J).

9) Significant auroral enhancements were also observed for NO^+ and CO_2 in the 4.3-μm region.

10) No auroral enhancements were found in the 11–13- or 18–22-μm window regions.

Acknowledgments

We dedicate this paper to the late Lacy Veach, one of the two mission specialists for the CIRRIS-1A mission, without whose dedication and hard work the CIRRIS experiment would not have achieved the level of success which it did. We are forever indebted to his efforts and to those of Col. Guy Bluford, our other mission specialist.

First, we especially thank the following people who made important contributions to this paper, which unfortunately we were unable to include as coauthors due to the author limit imposed by this journal. These are D. K. Zhou, formerly with Utah State University and now with NASA Langley Research Center; G. E. Bingham of Utah State University; and E. N. Richards and S. H. Delay of Boston College.

The overall high quality of the CIRRIS data and results was a direct result of a remarkable state-of-the-art sensor that operated flawlessly throughout the entire CIRRIS mission. For this we are forever indebted to E. R. Huppi and the superb and extremely dedicated team of scientists and engineers at the Space Dynamics Laboratory at Utah State University. Specifically, we thank S. Wellard, B. Bartschi, D. Morse, D. Ferguson, J. Blakeley, J. Petersen, and E. Vendell. We also are indebted to N. Bonito of RADEX Corporation, Bedford, Massachusetts, and C. Demars of Orbital Science Corporation, Chandler, Arizona.

The success of the CIRRIS-1A experiment required the dedicated commitment of many skilled people. Although it is not possible to thank everyone by name, the authors gratefully acknowledge the contributions of the following personnel and their organizations: A. T. Stair, formerly of the Air Force Geophysics Laboratory, under whose imagination and leadership the CIRRIS experiment was conceived; C. Fitz, who while at the Defense Nuclear Agency provided some of the initial financial support; W. Frederick, the late B. Katz, and Col. D. Heitz of the Space Defense Initiative Organization for their steadfast support and confidence in an idea that took 9 years to bear fruit; R. O'Neil, Maj. L. Vandiford, Maj. E. Imker, Capt. R. Doore, and Capt. D. Jacavanco for their outstanding management of the program; R. Steeves, who with J. Griffin and Capt. A. Landock of Phillips Laboratory led the test and evaluation team of Y. Baxter, W. Thorn, and J. Otis. These individuals, together with the sensor team at Utah State University (USU) and their subcontractors, ensured nearly trouble-free onorbit operation. Thanks also to R. Hegblom, T. Conley, W. Blumberg, R. Van Tassel, R. Sharma, and J. Winick who provided key mission planning and postflight data analysis support.

Special thanks to D. Caferelli, T. Codella, S. Osborne, and C. Roth, who together with other members of the flight operations team, pulled off a major success in interactive payload control. For the rapid turnaround and high-quality tape processing, we thank, R. McInerney, R. Raistrick, and A. Griffin.

Of the large team at USU's Space Dynamics Laboratory, the following people deserve special acknowledgment: K. Johnson and D. Hansen for keeping CIRRIS at its frigid best though the many years of ground testing; L. Bates for leading the cleaning effort;

S. Brown, L. Littledike, and D. John; and A. Steed, D. Burt, D. Baker, and B. Jensen, under whose leadership the USU effort has prospered. We also thank A. Bertino of Orbital Sciences Corporation; M. Anapol, D. Wang, J. Guregian, and B. Benoit for the design, care, and cleaning of the cryogenic high-rejection telescope.

Beyond the immediate CIRRIS family, there were many organizations and people who also made significant contributions to the CIRRIS effort. These include: Col. J. Armstrong, Maj. L. Johnson, Capt. M. Spencer, and Capt. P. Clark, who led the Air Force Space Systems Division Space Test Program team; H. Shodiss and the AFP-675 integration team at Lockheed Missiles and Space Company; E. Clark, D. Berrier, J. White, D. Chisolm, R. Agardy, and K. Mosher of The Aerospace Corporation for their excellent test and flight-operations support; former (astronaut) Mission Specialist designees Maj. P. Sefcheck, Maj. B. Waterson, Maj. R. Odle, Col. M. Mullane and Maj. J. Ross, who dedicated their collective efforts to improving the CIRRIS mission before the extended delay following the Challenger accident; the superb NASA integration, launch, and flight teams who made Discovery such an effective work place; and last but by no means least, the other members of the STS-39 crew, Cmdr. M. Coats, Pilot B. Hammond, and Mission Specialists D. McMonagle, R. Hieb, and G. Harbaugh.

References

[1]Baker, K. D., Baker, D. J., Ulwick, J. C., and Stair, A. T., Jr., "Rocketborne Measurements of an Infrared Enhancement Associated with a Bright Auroral Breakup," U.S. Air Force Geophysics Lab., AFGL-TR-77-0157, ERP 605, HAES Rept. 50, Hanscom AFB, MA, 1977, pp. 38–39.

[2]Stair, A. T., Jr., Ulwick, J. C., Baker, K. D., and Baker, D. J., "Rocketborne Observations of Atmospheric Infrared Emissions in the Auroral Region," *Atmospheres of Earth and the Planets*, D. Reidel, Dordrecht, The Netherlands, 1975, pp. 335–346.

[3]Stair, A. T., Jr., Pritchard, J., Coleman, I., Bohme, C., Williamson, W., Rogers, J., and Rawlins, W. T., "The Rocketborne Cryogenic (10°K) High-Resolution Interferometer Spectrometer Flight—HIRIS: Atmospheric and Auroral Infrared Emission Spectra," *Applied Optics*, Vol. 22, No. 7, 1983, pp. 1056–1069.

[4]Sharma, R. D., Nadile, R., Stair, A. T., Jr., and Gallery, W., "Earth Limb Emission of Spectral Infrared Rocket Experiment (SPIRE) Data at 2.7 Micrometers," *Modern Utililization of Infrared Technology VII*, *SPIE Proceedings*, Vol. 304, 1981, p. 139.

[5]Stair, A. T., Jr., Sharma, R. D., Nadile, R. M., Baker, D. J., and Greider, W. F., "Observations of Limb Radiance with Cryogenic Spectral Infrared Rocket Experiment," *Journal of Geophysical Research*, Vol. 90, No. A10, 1985, pp. 9763–9775.

[6]Ahmadjian, M., Bartschi, B., Nadile, R., and Wise, J. O., "CIRRIS-1A Space Shuttle Experiment," *Journal of Spacecraft and Rockets*, Vol. 27, No. 6, 1990, pp. 669–674.

[7]Ahmadjian, M., Bartschi, B. Y., Beeler, C. J., Blakely, J. G., Bluford, G. S., Blumberg, W., Conley, T. D., Dean, D. A., Dewan, E. M., Dodd, J., Gardiner, H., Grieder, W. F., Griffin, J. R., Healey, R., Humphrey, C. H., Huppi, E. R., Johnson, K., Lipson, S., Nadile, R. M., Pitkanen, M. E., Sharma, R., Steed, A. J., VanTassel, R. A., Veach, C. L., Wheeler, N. B., and Wise, J. O., "Observations of Infrared Backgrounds with the Cryogenic Infrared Radiance Instrumentation for Shuttle," *Proceedings of the 1992 Meeting of the IRIS Specialty Group on Targets, Backgrounds, and Discrimination*, Orlando, FL, Jan. 1992.

[8]Bartschi, B., Blakely, J., Brown, S., Huppi, E. R., and Wellard, S., "Cryogenic Michelson Interferometer on the Space Shuttle," *SPIE Proceedings*, Vol. 1765, July 1992.

[9]Bartschi, B., Steed, A., Blakely, J., Ahmadjian, M., Griffin, J., and Nadile, R., "Cryogenic Infrared Radiance Instrumentation for Shuttle (CIRRIS-1A) Instrumentation and Flight Performance," *SPIE Proceedings*, Vol. 1765, July 1992, pp. 64–74.

[10]Smith, D. R., Ratkowski, A. J., Adler-Golden, S. M., Matthew, M. W., Grieder, W. F., and Richards, E. N., "SPIRIT 1 Final Flight Report," U.S. Air Force Geophysics Lab., AFGL Environmental Research Papers, No. 1094, PL-TR-91-2226, Hanscom AFB, MA, 1991.

[11]Elwell, J. D., Kemp, J. C., and Larsen, K. D., "Quick-Look Analysis of the Spatial Infrared Rocketborne Interferometer Telescope II (SPIRIT II) Flight," Space Dynamics Lab., Rept. SDL/920028, Logan, UT, May 1992.

[12]Kemp, J. C., Larsen, K. D., and Huppi, E. R., "Rocketborne Spatial Radiometer—SPIRIT II," *Optical Engineering*, Vol. 33, No. 1, 1994, pp. 37–43.

[13]Ratkowski, A. J., Huppi, E. R., Akerstrom, D. S., and Austin, R. A., "Analysis of Data from the SPIRIT II Mission," *Proceedings of the 1994 Meeting of the IRIS Specialty Group on Targets, Backgrounds, and Discrimination*, Vol. 1, Monterey, CA, 1994, pp. 231–250.

[14]Mill, J. D., O'Neil, R. R., Price, S., Romick, G. J., Uy, O. M., Gaposchkin, E. M., Light, G. C., Moore, W. W., Jr., Murdock, T. L., and Stair, A. T., Jr., "Midcourse Space Experiment," *Journal of Spacecraft and Rockets*, Vol. 31, No. 5, 1994, pp. 900–907.

[15]Smith, D. R., "Evidence for Off-Axis Leakage Radiance in High Altitude IR Rocketborne Measurements, Stray Light and Contamination in Optical Systems," *SPIE Proceedings*, Vol. 967, 1988, pp. 30–36.

[16]Wheeler, N. B., Smith, D. R., Dean, D., Gardiner, H., Gibson, J., Griffin, J., Price, S., Nadile, R., Bates, L., Bingham, G., Johnson, K., Guregian, J., and Benoit, R., "An Assessment of the Near-Field Contamination and Off-Axis Leakage Effects on Earthlimb Background Measurements from CIRRIS-1A," *SPIE Proceedings*, Vol. 1754, 1992, pp. 156–168.

[17]Wheeler, N. B., Nadile, R., Gardiner, H. A. B., Gibson, J., Bates, L., Guregian, J., and Benoit, B., "CIRRIS Mirror Cleaning History Review," U.S. Air Force Phillips Lab., Rept. PL-TR-91-2166, Environmental Research Papers, No. 1087, Hanscom AFB, MA, July 1991.

[18]Grieder, W. F., and Foley, C. I., "Conpendium of Earth Limb Infrared Background Measurements from SPIRE," U.S. Air Force Geophysics Lab., Rept. AFGL-TR-82-0326, Hanscom AFB, MA, 1982.

[19]Adler-Golden, S. M., Smith, D. R., and Matthew, M. W., "Atmospheric Infrared Radiance from CO_2 and NO Observed During the SPIRIT I Rocket Experiment," *Journal of Geophyical Research*, Vol. 96, No. A7, 1991, pp. 11,319–11,329.

[20]Bingham, G., Peterson, J., Brown, S., Morse, D., Bartschi, B., and Steed, A., "CIRRIS-1A Post-Flight Calibration Final Report," Vols. 1 and 2, Space Dynamics Lab., Rept. SDL/92-091, Utah State Univ., Logan, UT, 1992.

[21]Bingham, G., Peterson, J., Brown, S., Morse, D., Bartschi, B., and Steed, A., "CIRRIS-1A Post-Flight Calibration," U.S. Air Force Phillips Lab., Rept. PL-TR-2037 (I), Hanscom AFB, MA, 1995.

[22]Bingham, G. E., Zhou, D. K., Bartschi, B. Y., Anderson, G. P., Smith, D. R., Chetwynd, J. H., and Nadile, R. M., "Cryogenic Infrared Radiance Instrumentation for Shuttle (CIRRIS 1A) Earth Limb Spectral Measurements, Calibration, and atmospheric O_3, HNO_3, CFC-12, and CFC-11 Profile Retrieval," *Journal of Geophysical Research*, Vol. 102, No. D3, 1997, pp. 3547–3558.

[23]Nadile, R. M., Ahmadjian, M., Blumberg, W., Dean, D., Griffin, J., Huppi, R., Sharma, R., Smith, D., Van Tassel, R., Wheeler, N., Wise, J., Hegblom, R., Conley, T., Steed, A., Bartschi, B., Morse, D., Wellard, S., Bingham, G., Bluford, G., and Veach, L., "Observations of Infrared Backgrounds with the Cryogenic Infrared Radiance Instrumentation for Shuttle (CIRRIS-1A) from STS-39," *Proceedings of 1992 Meeting of the IRIS Specialty Group on Targets, Backgrounds, and Discrimination*, Logan, UT, Jan. 1992.

[24]Dodd, J. A., Winick, J. R., Blumberg, W. A. M., Lipson, S. J., Armstrong, P. S., and Lowell, J. R., "CIRRIS-1A Observation of $^{13}C^{16}O$ and $^{12}C^{18}O$ Fundamental Band Radiance in the Upper Atmosphere," *Geophysical Research Letters*, Vol. 20, No. 23, 1993, pp. 2683–2686.

[25]Smith, D. R., Blumberg, W. A. M., Nadile, R. M., Lipson, S. J., Huppi, E. R., Wheeler, N. B., and Dodd, J. A., "Observation of High-N Hydroxyl Pure Rotation Lines in Atmospheric Emission Spectra by the CIRRIS lA Space Shuttle Experiment," *Geophysical Research Letters*, Vol. 19, No. 6, 1992, pp. 593–596.

[26]Dodd, J. A., Blumberg, W. A. M., Lipson, S. J., Lowell, J. R., Armstrong, P. S., Smith, D. R., Nadile, R. M., Wheeler, N. B., and Huppi, E. R., "OH(v, N) Column Densities from High-Resolution Earthlimb Spectra," *Geophysical Research Letters*, Vol. 20, No. 4, 1993, pp. 305–308.

[27]Rappaport, S. A., Rieder, R. J., Reidy, W. P., McNutt, R. I., Jr., Atkinson, J. J., and Paulsen, D. E., "Remote X-Ray Measurements of the Electron Beam from the EXCEDE III Experiment," *Journal of Geophysical Research*, Vol. 98, No. A11, 1993, pp. 19,093–19,098.

[28]Zachor, A., and Sharma, R. D., "Retrieval of Non-LTE Vertical Structure from a Spectrally Resolved Infrared Limb Radiance Profile," *Journal of Geophysical Research*, Vol. 90, No. A1, 1985, pp. 467–475.

[29]Dean, D. A., Healey, R., Huppi, E. R., Lowell, J., Nadile, R., Sharma, R., Smith, D., and Wheeler, N., "Near-Field Water Vapor Contamination Observed on STS-39," *SPIE Proceedings*, Vol. 1754, 1992, pp. 148–155.

[30]Dean, D. A., Huppi, E. R., Smith, D. R., Nadile, R. M., and Zhou, D. K., "Space Shuttle Observations of Collisionally Excited Outgassed Water Vapor," *Geophysical Research Letters*, Vol. 21, No. 7, 1994, pp. 609–612.

[31]Zhou, D. K., Pendleton, W. R., Bingham, G. E., Steed, A. J., and Dean, D. A., "Infrared Spectral Measurements (450–2500 cm^{-1}) of Shuttle-Induced Optical Contamination," *Geophysical Research Letters*, Vol. 21, No. 7, 1994, pp. 613–616.

[32]Zhou, D. K., Pendleton, W. R., Jr., Bingham, G. E., Steed, A. J., and Nadile, R. M., "Shuttle-Induced Optical Contamination Observed from STS-39 by CIRRIS-1A," *EOS Transactions*, American Geophysical Union, Vol. 74, No. 43, Fall Meeting Suppl., 1993, p. 467.

[33]Makhlouf, U. B., Picard, R. H., and Winick, J. R., "Photochemical-Dynamical Modeling of the Measured Response of Airglow to Gravity

Waves. 1. Basic Model for OH Airglow," *Journal of Geophysical Research*, Vol. 100, No. D9, 1995, pp. 11,289–11,311.

[34]Wise, J. O., Carovillano, R. L., Carlson, H. C., Roble, R. G., Adler-Golden, S., Nadile, R. M., and Ahmadjian, M., "CIRRIS 1A Global Observation of 15-μm CO_2 and 5.3-μm NO Limb Radiance in the Lower Thermosphere During Model Rate to Active Geomagnetic Activity," *Journal of Geophysical Research*, Vol. 100, No. A11, 1995, pp. 21,357–21,373.

[35]Smith, D. R., and Ahmadjian, M., "Observation of Nitric Oxide Rovibrational Band Head Emissions in the Quiescent Airglow During the CIRRIS-1A Space Shuttle Experiment," *Geophysical Research Letters*, Vol. 20, No. 23, 1993, pp. 2679–2682.

[36]Armstrong, P. S., Lipson, S. J., Dodd, J. A., Lowell, J. R., Blumberg, W. A. M., and Nadile, R. M., "Highly Rotationally Excited NO (v, J) in Thermosphere from CIRRIS-1A Limb Radiance Measurements," *Geophysical Research Letters*, Vol. 21, No. 22, 1994, pp. 2425–2428.

[37]Sharma, R. D., Dothe, H., von Esse, F., Kharchenko, V. A., Sun, Y., and Dalgarno, A., "Production of Vibrationally and Rotationally Excited NO in the Nighttime Terrestrial Themosphere," *Journal of Geophysical Research*, Vol. 101, No. A9, 1996, pp. 19,707–19,713.

[38]Rothman, L. S., Gamache, R. R., Tipping, R. H., Rinsland, C. P., Smith, M. A. H., Chris Benner, D., Malathy Devi, V., Flaud, J.-M., Camy-Peyret, C., Perrin, A., Goldman, A., Massie, S. T., Brown, L. R., and Toth, R. A., "The HITRAN Molecular Database: Editions of 1991 and 1992," *Journal of Quantitative Spectroscopy and Radiative Transfer*, Vol. 48, No. 5–6, 1992, pp. 469–507.

[39]Adler-Golden, S., Smith, D. R., Vail, J., Berk, A., Nadile, R., and Jeong, L., "Simulations of Mesospheric and Thermospheric IR Radiance Measured in the CIRRIS-1A Shuttle Experiment," *Journal of Atmospheric and Solar-Terrestrial Physics*, Vol. 61, 1999, pp. 1397–1410.

[40]Lipson, S. J., Armstrong, P. S., Blumberg, W. A. M., Dodd, J. A., Lowell, J. R., and Nadile, R. M., "Subthermal Nitric Oxide Spin-Orbit Distributions in the Thermosphere," *Geophysical Research Letters*, Vol. 21, No. 22, 1994, pp. 2421–2424.

[41]Sharma, R. D., Wheeler, N. B., Wise, J. O., Dothe, H., and Duff, J. W., "Global Variations in the 2.7 μm NO Overtone Limb-Emission from the Lower Thermospere," *Geophysical Research Letters*, Vol. 27, No. 3, 2000, pp. 349–352.

[42]Paulsen, D. E., Armstrong, P. S., Lipson, S. J., Lowell, J., Blumberg, W., Fraser, M., Rawlins, W. T., Green, B. D., Murphy, R., Bien, F., Duff, J. W., Rieder, R., Armstrong, R. A., and Bruce, M., "Overview of Infrared Observations from EXCEDE III," *Proceedings of the 1994 Meeting of the IRIS Specialty Group on Targets Backgrounds and Discrimination*, Vol. 1, Monterey, CA, 1994, pp. 91–109.

[43]Sharma, R. D., Dothe, H., and Von Esse, F., "On the Rotational Distribution of the 5.3-μm Thermal Emission from Nitric Oxide in the Terrestrial Thermosphere," *Journal of Geophysical Research*, Vol. 101, No. A8, 1996, pp. 17,129–17,135.

[44]Dothe, H., Von Esse, F., and Sharma, R. D., "Rotational Temperatures and Production Mechanisms of Some Infrared Radiators in the Daylit Terrestrial Thermosphere," *Journal of Geophysical Research*, Vol. 101, No. A9, 1996, pp. 19,715–19,721.

[45]Duff, J. W., and Sharma, R. D., "On the Retrieval of the Nighttime Thermospheric Temperature from NO ($v = 1$) 5.3 μm Emission," *SPIE Proceedings*, Vol. 3220, 1997, pp. 222–228.

[46]Sharma, R. D., and Duff, J. W., "Determination of the Translational Temperature of the High Altitude Terrestrial Thermosphere from the Rotational Distribution of the 5.3 μm Emission from NO ($v = 1$)," *Geophysical Research Letters*, Vol. 24, No. 19, 1997, pp. 2407–2410.

[47]Smith, D. R., "Observation of Highly Rotationally Excited Airglow Emissions from the Overtone Band of NO in the Thermosphere," *Journal of Atmospheric and Solar-Terrestrial Physics* (submitted for publication).

[48]Picard, R. H., Winick, J. R., Sharma, R. D., Zachor, A. S., Espy, P. J., and Harris, C. R., "Interpretation of Infrared Measurements of the High-Latitude Thermosphere from a Rocket-Borne Interferometer," *Advances in Space Research*, Vol. 7, No. 10, 1987, pp. 23–30.

[49]Espy, P. J., Harris, C. R., Steed, A. J., Ulwick, J. C., Haycock, R. H., and Straka, R., "Rocketborne Interferometer Measurement of Infrared Auroral Spectra," *Planetary and Space Science*, Vol. 36, No. 6, 1988, pp. 543–551.

[50]Picard, R. H., Lee, E. T. P., Winick, J. R., Smith, D. R., Nadile, R. M., Paboojian, A. J., and Wintersteiner, P. P., "STS-39 Measurements of 4.3 μm Earthlimb Emission from CO_2 and NO^+," *EOS Transactions*, Vol. 73, No. 14, 1992, p. 222.

[51]Winick, J. R., "Analysis of the 4.3 μm Limb Emission Observed by STS-39," *EOS Transactions*, Vol. 73, No. 43, 1992, p. 418.

[52]Caledonia, G. E., Murphy, R. E., Nadile, R. M., and Ratkowski, A. J., "Analysis of Auroral Infrared Emissions Observed During the ELIAS Experiment," *Annales Geophysicae*, Vol. 13, No. 3, 1995, pp. 247–252.

[53]Smith, D. R., Huppi, E. R., and Wise, J. O., "Observation of Highly Rotationally Excited NO^+ Emissions in the Thermosphere," *Journal of Atmospheric and Solar-Terrestrial Physics*, Vol. 62, April 2000, pp. 1189–1198.

[54]Zhou, D. K., Mlynczak, M. G., Bingham, G. E., Wise, J. O., and Nadile, R. M., "CIRRIS-1A Limb Spectral Measurements of Mesospheric 9.6-μm Airglow and Ozone," *Journal of Geophysical Research*, Vol. 25, No. 5, 1998, pp. 643–646.

[55]Solomon, S., Rusch, D. W., Thomas, R. J., and Eckman, R. S., "Comparison of Mesospheric Ozone Abundances Measured by the Solar Mesospheric Explorer and Model Calculations," *Geophysical Research Letters*, Vol. 10, No. 4, 1983, pp. 249–252.

[56]Gunson, M. R., Farmer, C. B., Norton, R. H., Zander, R., Rinsland, C. P., Shaw, J. H., and Gao, B.-C., "Measurements of CH_4, N_2O, CO, H_2O, and O_3 in the Middle Atmosphere by the Atmospheric Trace Molecule Spectroscopy Experiment on Spacelab 3," *Journal of Geophysical Research*, Vol. 95, No. 9, 1990, pp. 13,867–13,882.

[57]Rawlins, W. T., Woodward, A. M., and Smith, D. R., "Aeronomy of Infrared Ozone Fluorescence Measured During an Aurora by the Spirit 1 Rocketborne Interferometer," *Journal of Geophysical Research*, Vol. 98, No. A3, 1993, pp. 3677–3691.

[58]Garcia, R. R., and Solomon, S., "A New Numerical Model of the Middle Atmosphere, 2: Ozone and Related Species," *Journal of Geophysical Research*, Vol. 99, No. 6, 1994, pp. 12,937–12,951.

[59]Lowell, J. R., Lipson, S. J., Blumberg, W. A. M., Armstrong, P. S., Dodd, J. A., Green B. D., and Rawlins, W. T., "Analysis of CIRRIS 1A Ozone Spectra in the 9.6 and 4.7 μm Regions," *EOS Transactions*, Vol. 74, No. 43, 1993, p. 467.

[60]Dodd, J. A., Lipson, S. J., Lowell, J. R., Armstrong, P. S., Blumberg, W. A. M., Nadile, R. M., Adler-Golden, S. M., Marinelli, W. J., Holtzclaw, K. W., and Green, B. D., "Analysis of Hydroxyl Earthlimb Airglow Emissions: Kinetic Model for State-to-State Dynamics of OH(v, N)," *Journal of Geophysical Research*, Vol. 99, No. D2, 1994, pp. 3559–3585.

[61]Kaye, J. A., "On the Possible Role of the Reaction $O + HO_2 \rightarrow OH + O_2$ in OH Airglow," *Journal of Geophysical Research*, Vol. 93, No. 1, 1988, pp. 285–288.

[62]Zhou, D. K., Bingham, G. E., Rezai, B. K., Anderson, G. P., Smith, D. R., and Nadile, R. M., "Stratospheric CH_4, N_2O, H_2O, NO_2, N_2O_5, and $ClONO_2$ Profiles Retrieved from Cryogenic Infrared Radiance Instrumentation for Shuttle (CIRRIS-1A)/STS-39 Measurements," *Journal of Geophysical Research*, Vol. 102, No. D3, 1997, pp. 3559–3573.

[63]Zhou, D. K., Bingham, G. E., Anderson, G. P., and Nadile, R. M., "CIRRIS-1A Measurements of Stratospheric Carbon Tetrachloride (CCl_4) and Carbon Tetrafluoride (CF_4)," *Geophysical Research Letters*, Vol. 25, No. 3, 1998, pp. 325–328.

[64]Miller, S. M., Snell, H. E., and Moncet, J.-L., "Simultaneous Retrieval of Middle Atmospheric Temperature and Trace Gas Species Volume Mixing Ratios from CIRRIS-1A," *Journal of Geophysical Research*, Vol. 104, No. 15, 1999, pp. 18,697–18,714.

[65]Clough, S. A., Kneizys, F. X., Anderson, G. P., Shettle, E. P., Chetwynd, J. H., Abreu, L. W., Hall, L. A., and Worsham, R. D., "FASCOD3: Spectral Simulation, in IRS'88: Current Problem in Atmospheric Radiation," *Proceedings of the 1988 International Radiation Symposium*, edited by J. Lenoble, J.-F. Geleyn, and A. Deepak, Hampton, VA, 1989, pp. 372–375.

[66]Rothman, L. S., Rinsland, C. P., Goldman, A., Massie, S. T., Edwards, D. P., Flaud, J.-M., Perrin, A., Camy-Peyret, C., Dana, V., Mandin, J.-Y., Schroeder, J., McCann, A., Gamache, R. R., Wattson, R. B., Yoshino, K., Chance, K. V., Jucks, K. W., Brown, L. R., Nemtchinov, V., and Varanasi, P., "The HITRAN Molecular Spectroscopic Database and HAWKS (HITRAN Atmospheric Workstation): 1996 Edition," *Journal of Quantitative Spectroscopy and Radiative Transfer*, Vol. 60, No. 5, 1998, pp. 665–710.

[67]Miller, S. M., Winick, J., and Snell, H. E., "Non-LTE Effects on Retrieval of Temperature from the CO_2 Laser Bands Using CIRRIS-1A Data," *Journal of Geophysical Research*, Vol. 105, No. D8, 2000, pp. 10,193–10,202.

[68]Roche, A. E., "Observation of Lower Stratospheric $ClONO_2$, NHO_3 and Aerosol by the UARS CLAES Experiment Between January and April 1993," *Journal of Atmospheric Science*, Vol. 51, No. 20, 1994, pp. 2877–2902.

[69]Rinsland, C. P., Gunson, M. R., Abrams, M. C., Lowes, L. L., Zander, R., Mahieu, E., Goldman, A., Ko, M. K. W., Rodriguez, J. M., and Sze, N. D., "Heterogeneous Conversion of N_2O_5 to HNO_3 in the Post-Mount Pinatubo Eruption Stratosphere," *Journal of Geophysical Research*, Vol. 99, No. D4, 1994, pp. 8213–8219.

[70]Spreng, S., and Arnold, F., "Balloon-Borne Mass Spectrometer Measurements of HNO_3 and HCN in the Winter Arctic Stratosphere—Evidence for HNO_3-Processing by Aerosols," *Geophysical Research Letters*, Vol. 21, No. 13, 1994, pp. 1251–1254.

[71]Russell, J. M., III, Gille, J. C., Remsberg, E. E., Gordley, L. L., Bailey, P. L., Drayson, S. R., Fischer, H., Girard, A., Harries, J. E., and Evans, W. F. J., "Validation for Nitrogen Dioxide Results Measured by the Limb Infrared Monitor of the Stratosphere (LIMS) Experiment on Nimbus 7," *Journal of Geophysical Research*, Vol. 89, No. 4, 1984, pp. 5099–5107.

[72]Russell, J. M., III, Solomon, S., Gordley, L. L., Remsberg, E. E., and Callis, L. B., "The Variability of Stratospheric and Mesospheric NO_2 in the

Polar Winter Night Observed by LIMS," *Journal of Geophysical Research*, Vol. 89, No. 5, 1984, pp. 7267–7275.

[73]Gille, J. C., Russell, J. M., III, Bailey, P. L., Remsberg, E. E., Gordley, L. L., Evans, W. F. J., Fischer, H., Gandrud, B. W., Girard, A., Harries, J. E., and Beck, S. A., "Accuracy and Precision of Nitric Acid Concentrations Determined by the Limb Infrared Monitor of the Stratosphere Experiment on Nimbus 7," *Journal of Geophysical Research*, Vol. 89, No. 4, 1984, pp. 5179–5190.

[74]Russell, J. M., III, Farmer, C. B., Rinsland, C. P., Zandler, R., Froidevaux, L., Toon, G. C., Gao, B., Shaw, J., and Gunson, M., "Measurements of Odd Nitrogen Compounds in the Stratosphere by the ATMOS Experiment on Spacelab 3," *Journal of Geophysical Research*, Vol. 93, No. 2, 1988, pp. 1718–1736.

[75]Rinsland, C. P., Toon, G. C., Farmer, C. B., Norton, R. H., and Namkung, J. S., "Stratospheric N_2O_5 Profiles at Sunrise and Sunset from Further Analysis of the ATMOS/Spacelab 3 Solar Spectra," *Journal of Geophysical Research*, Vol. 94, No. 15, 1989, pp. 18,341–18,349.

[76]Reber, C. A., Trevathan, C. E., McNeal, R. J., and Luther, M. R., "The Upper Atmosphere Research Satellite (UARS) Mission," *Journal of Geophysical Research*, Vol. 98, No. D6, 1993, pp. 10,643–10,647.

[77]Pyle, J. A., Harris, N. R. P., Farman, J. C., Amold, F., Braathen, G., Cox, R. A., Faucon, P., Jones, R. L., Megie, G., O'Neill, A., Platt, U., Pommereau, J- P., Schmidt, U., and Stordal, F., "An Overview of the EASOE Campaign," *Geophysical, Research Letters*, Vol. 21, No. 13, 1994, pp. 1191–1194.

[78]Goldan, P. D., Kuster, W. C., Albritton, D. L., and Schmeltekopf, A. L., "Stratospheric $CFCl_3$, CF_2Cl_2, and N_2O Height Profile Measurements at Several Latitudes," *Journal of Geophysical Research*, Vol. 85, No. C1, 1980, pp. 413–423.

[79]Cunnold, D. M., Prinn, R. G., Rasmussen, R. A., Simmonds, P. G., Alyea, F. N., Cardelino, C. A., Crawford, A. J., Fraser, P. J., and Rosen, R. D., "The Atmospheric Lifetime Experiment, 3: Lifetime Methodology and Application to Three Years of $CFCl_3$ Data," *Journal of Geophysical Research*, Vol. 88, No. C13, 1983, pp. 8379–8400.

[80]Cunnold, D. M., Prinn, R. G., Rasmussen, R. A., Simmonds, P. G., Alyea, F. N., Cardelino, C. A., and Crawford, A. J., "The Atmospheric Lifetime Experiment, 4: Results for CF_2Cl_2 Based on Three Years Data," *Journal of Geophysical Research*, Vol. 88, No. C13, 1983, pp. 8401–8414.

[81]Zander, R., Rinsland, C. P., Farmer, C. B., and Norton, R. H., "Infrared Spectroscopic Measurements of Halogenated Source Gases in the Stratosphere with the ATMOS Instrument," *Journal of Geophysical Research*, Vol. 92, No. 8, 1987, pp. 9836–9850.

[82]Watson, R. T., Prather, M. J., and Kurylo, M. J., "Present State of Knowledge of the Upper Atmosphere 1988: An Assessment Report," NASA Reference Publ. Vol. 1208, 1988, pp. 1–208.

[83]Prather, M. J., and Watson, R. T., "Stratospheric Ozone Depletion and Future Levels of Atmospheric Chlorine and Bromine," *Nature*, Vol. 344, No. 6268, 1990, pp. 729–733.

[84]Von Clarmann, T., Fischer, H., and Oelhaf, H., "Retrieval of Atmospheric O_3, HNO_3, CFC-11 and CFC-12 Profiles from MIPAS-B-89 Limb Emission Spectra," *Applied Optics*, Vol. 32, No. 33, 1993, pp. 6808–6817.

[85]Plumb, R. A., and Ko, M. K. W., "Interrelationship Between Mixing Ratios of Long-Lived Stratospheric Constituents," *Journal of Geophysical Research*, Vol. 97, No. D9, 1992, pp. 10,145–10,156.

[86]Rawlins, W. T, Caledonia, G. E., Gibson, J. J., and Stair, A. T., Jr., "HIRIS Rocketborne Spectra of Infrared Fluorescence in the $O_3(\upsilon_3)$ Band Near 100 km," *Journal of Geophysical Research*, Vol. 90, No. A3, 1985, pp. 2896–2904.

[87]Smith, D. R., Nadile, R. M., Richards, E., Hegblom, R., and Gibson, R., "Diurnal Variability of IR Emission Profiles Near the Terminator as Observed by the CIRRIS-1A Experiment from the Space Shuttle," *EOS Transactions*, Vol. 73, No. 43, 1992, p. 222.

[88]Conley, T. D., Hegblom, E. R., Grieder, W. F., Beeler, C. J., Humphrey, C. H., Nadile, R. M., VanTassel, R. A., and Huppi, E. R., "CIRRIS 1A Measurements of BTH Backgrounds in the SWIR and MWIR Wavelength Regions," *Proceedings of the 1992 Meeting of the IRIS Specialty Group on Targets, Backgrounds, and Discrimination*, Orlando, FL, Jan. 1992.

[89]Conley, T. D., Hegblom, E. R., Stern, I., Sears, R., Nadile, R., and Van Tassel, R., "An MWIR Model for BTH Backgrounds," *Proceedings of the IRIS Specialty Group on Targets, Backgrounds, and Discrimination*, Monterey, CA, Feb. 1994.

[90]Grieder, W. F., Conley, T. D., Manolakis, D., Stern, I., Nadile, R. M., and Van Tassel, R. A., "Fractal-Based Description of CIRRIS 1A and IBSS BTH Measurements," *Proceedings of the IRIS Specialty Group on Targets, Backgrounds, and Discrimination*, San Antonio, TX, Jan. 1993.

[91]Sears, R. D, Conley, T. D., Stern, I., Strugala, L. A., Newt, J. E., Nadile, R., and Van Tassel, R., "CIRRIS 1A Earthlimb Clutter Results: Comparison with Models and System Implicatioins," *Proceedings of the IRIS Specialty Group on Targets, Backgrounds, and Discrimination*, San Antonio, TX, Jan. 1993.

[92]Sears, R. D., Conley, T. D., Stern, I., Nadile, R., and Van Tassel, R., "New Results of the CIRRIS-1A Earthlimb Clutter Comparisons with Structure Models," *Proceedings of the IRIS Specialty Group on Targets, Backgrounds, and Discrimination*, Monterey, CA, Feb. 1994.

[93]Shanks, J., Mertz, F. C., Nadile, R. M., and Conley, T. D., "A Detailed Comparison of CLDSIM Predictions with CIRRIS 1A Radiometer Data in SWIR and MWIR Spectral Bands," *Cloud Impacts on DOD Operations and Systems 1993 Conference*, Fort Belvoir, VA, Nov. 1993.

[94]Manolakis, D., Conley, T., Wilson, R., Nadile, R. M., Ahmadjian, M., Shanks, J., and Mertz, F., "A Comparison of Visible and IR Imagery," *Proceedings of the 1994 Meeting of the IRIS Specialty Group on Targets, Backgrouds, and Discrimination*, Vol. 1, Monterey, CA, 1994.

[95]Van Tassel, R. A., Blumberg, W. A. M., Jeong, L. S., Nadile, R. M., Sharma, R. D., Huppi, E. R., Brown, J. H., Gruninger, J. H., Sundberg, R. L., De, P., Robertson, D. C., Sears, R. D., Thornburg, R., DeVore, J., Stephens, T., Beeler, C. J., and Huppi, R. J., "Spatially Structured Earthlimb Backgrounds: Model and Measurements Update," *Proceedings of the IRIS Specialty Group on Targets, Backgrounds, and Discrimination*, Vol. 2, Cocoa Beach, FL, 1995.

[96]Bechman, C. A., Neugebauer, G., Habing, H. J., Clegg, P. E., and Chester, T. J. (ed.), *Infrared Astronomical Satellite Catalogs and Atlases*, 2nd ed., Joint Infrared Astronomy Satellite Science Working Group, NASA, Washington, DC, 1988.

[97]Taylor, S., Morris, D., and Hamilton, C., "SPIRIT III Convert 5.0 Certification Report," Frontier Technology, Inc., Rept. 6140-98-02-TR, Danvers, MA, April 1998, pp. 11, 12.

[98]Narcisi, M. M., Trzcinski, E., Federico, G., Wloydka, L., and Delorey, D., "The Gaseous and Plasma Environment Around the Space Shuttle," U.S. Air Force Geophysics Lab., Rept. AFGL-TR-83-2659, Hanscom AFB, MA, 1983.

[99]Carignan, G. R., and Miller, E. R., "Mass Spectrometer in STS-2, 3, 4 Induced Environment Contamination Monitor Summary Report," NASA TM-82524, Feb. 1983.

[100]Banks, P. M., Williamson, P. R., and Raitt, W. J., "Space Shuttle Glow Observations," *Geophysical Research Letters*, Vol. 10, No. 2, 1983, pp. 118–121.

[101]Simpson, J. P., and Witteborn, F. C., "Effect of the Shuttle Contaminant Environment on a Sensitive Infrared Telescope," *Applied Optics*, Vol. 16, No. 8, 1977, pp. 2051–2073.

[102]Green, B. D., Caledonia, G. E., and Wilkerson, T. D., "The Shuttle Environment: Gases, Particulates, and Glow," *Journal of Spacecraft and Rockets*, Vol. 22, No. 5, 1985, pp. 500–511.

[103]Young, S. J., and Herm, R. R., "Model for Radiation Contamination by Outgassing from Space Platforms," *Journal of Spacecraft and Rockets*, Vol. 25, No. 6, 1988, pp. 413–419.

[104]Torr, M. R., and Torr, D. G., "Gas Phase Collisional Excitation of Infrared Emission in the Vicinity of the Space Shuttle," *Geophysical Research Letters*, Vol. 15, No. 1, 1988, pp. 95–98.

[105]Elgin, J. B., Cooke, D. C., Tautz, M. F., and Murad, E., "Modeling of Atmospherically Induced Gas Phase Optical Contamination from Orbiting Spacecraft," *Journal of Geophysical Research*, Vol. 95, No. A8, 1990, pp. 12,197–12,208.

[106]Koch, D. G., Fazio, G. G., Hoffmann, W., Melnick, G., Rirke, G., Simpson, J., Witteborn, F., and Young, E., "Infrared Observations of Contaminants from Shuttle Flight 51-F," *Advances in Space Research*, Vol. 7, No. 5, 1987, pp. 211–221.

[107]Camy-Peyret, C., and Flaud, J.-M., "Line Positions and Intensities in the υ_2 Band of H_2O," *Molecular Physics*, Vol. 32, No. 2, 1976, pp. 523–537.

[108]Mandin, J.-Y., Dana, V., Camy-Peyret, C., and Flaud, J.-M., "Collisional Widths of Pure Rotational Transitions of H_2O from Fourier-Transform Flame Spectroscopy," *Journal of Molecular Spectroscopy*, Vol. 152, No. 1, 1992, pp. 179–184.

[109]Zhou, D. K., Pendleton, W. R., Jr., Bingham, G. E., Thompson, D. C., Raitt, W. J., and Nadile, R. M., "IR Excitation of Contaminant Water by Oxygen for the Space Shuttle at Low Earth Orbit Altitude," *Journal of Geophysical Research*, Vol. 99, No. A10, 1994, pp. 19,585–19,595.

[110]Green, B., Nadile, R., Rawlins, W. T., Uy, O. M., and Wheeler, N., "Contamination Signatures Observed During the CIRRIS-1A Mission," Society of Photo-Optical Instrumentation Engineers, *SPIE Proceedings*, Vol. 1754, July 1992, pp. 114–123.

[111]Goldman, A., Gillis, J. R., and Coxon, J. A., "Spectral Line Parameters for the Pure Rotation Bands of Solar OH," *Journal of Quantum Spectroscopy and Radiative Transfer*, Vol. 29, No. 5, 1983, pp. 469, 470.

[112]Kutepov, A. A., Oelhaf, H., and Fischer, H., "Non-LTE Radiative Transfer in the 4.7 μm Band of CO: Vibrational-Rotational Non-LTE and Its Effects on Limb Radiance," *Proceedings of the International Radiance Symposium*, 1992, pp. 548–551.

[113]Holtzclaw, K. W., Upschulte, B. L., Caledonia, G. E., Cronin, J. F., Green, B. D., Lipson, S. J., Blumberg, W. A. M., and Dodd, J. A., "Rotational Relaxation of High-N States of $OH(X^2\Pi, \upsilon = 1\text{–}3)$ by O_2," *Journal*

of Geophysical Research, Vol. 102, No. A3, 1997, p. 4521.

[114] Adler-Golden, S. M., "Kinetic Parameters for OH Nightglow Modeling Consistent with Recent Laboratory Measurements," *Journal of Geophysical Research*, Vol. 102, No. A9, 1997, pp. 19,969–19,976.

[115] Sharma, R. D., Sun, Y., and Dalgarno, A., "Highly Rotationally Excited Nitric Oxide in the Terrestrial Thermosphere," *Geophysical Research Letters*, Vol. 20, 1993, pp. 2043–2046.

[116] Sharma, R. D., Dothe, H., and Duff, J. W., "Model of the 5.3 μm Radiance from NO During the Sunlit Terrestrial Thermosphere," *Journal of Geophysical Research*, Vol. 103, No. A7, 1998, pp. 14,753–14,768.

[117] Duff, J. W., Bien, F., and Paulsen, D. E., "Classical Dynamics of the $N(^4S) + O_2 \rightarrow NO + O(^3P)$ Reaction," *Geophysical Research Letters*, Vol. 21, No. 18, 1994, pp. 2043–2046.

[118] Hubert, B., Gerard, J.-C., Bisikalo, D. V., and Shermatovich, V. I., "High Rotational Excitation of NO Infrared Thermospheric Airglow, A Signature of Superthermal Nitrogen Atoms?," *Geophysical Research Letters*, Vol. 23, No. 17, 1996, pp. 2215–2218.

[119] Duff, J. W., and Sharma, R. D., "Quasiclassical Trajectory Study of the $N(^4S) + NO(X^2\Pi) \rightarrow N_2(X^1\Sigma_g^+) + O(^3P)$ Reaction Rate Coefficient," *Geophysical Research Letters*, Vol. 23, No. 20, 1996, pp. 2777–2780.

[120] Duff, J. W., and Sharma, R. D., "Quasiclassical Trajectory Study of NO Relaxation by Collisions with Atomic Oxygen," *Journal of Chemical Society, Faraday Transactions*, Vol. 93, No. 16, 1997, pp. 2645–2649.

[121] Duff, J. W., and Sharma, R. D., "Quasiclassical Trajectory Study of the $N(^4S) + NO(X^2\Pi) \rightarrow N_2(X^1\Sigma_g^+) + O(^3P)$ Reaction Cross Section on the Excited $^3A'$ NNO Surface," *Chemical Physics Letters*, Vol. 265, No. 3–5, 1997, pp. 404–409.

[122] Dothe, H., Sharma, R. D., and Duff, J. W., "On the Steady-State Assumption for the Energy Distribution Function of the Nonthermal $N(^4S)$ Atoms and the Efficiency of NO Production by These Atoms in the Terrestrial Thermosphere," *Geophysical Research Letters*, Vol. 24, No. 24, 1997, pp. 3233–3236.

[123] Duff, J. W., and Smith, D. R., "The $O^+(^4S) + N_2(X^1\Sigma^+) \rightarrow NO^+(X^1\Sigma^+) + N(^4S)$ Reaction as a Source of Highly Rotationally Excited NO^+ in the Thermosphere," *Journal of Atmospheric and Solar-Terrestrial Physics*, Vol. 62, April 2000, pp. 1199–1206.

A. C. Tribble
Associate Editor